TOWARD ACTIVE CONTROL OF NOISE
FROM HOT SUPERSONIC JETS

Quarterly Progress Report No. 2

1 NOV 2011 – 31 JAN 2012

Nathan E. Murray (PI)
Aeroacoustics Research Group
National Center for Physical Acoustics
University of Mississippi
University, MS 38677
(662) 915-3190
nmurray@olemiss.edu

Contract: N00014-11-1-0752

Executive Summary

Significant progress has been made on WBS 1.0 and 2.0 items. The MHz PIV system has arrived at NCPA and successfully passed initial system check-out. The near-field microphone array has been built and tested in the UT Austin facility. The specific nozzle hardware to be used for the program has been identified, and mean profile measurements have been completed at the NCPA. CRAFT Tech has completed LES computations of one of the configurations of interest. Graduate students are heavily involved in the activities of each of the academic institutions. The plan for completion of the experimental data collection has been laid out to be completed by the end of the current academic year.

20120221003

15 February 2012

REPORT DOCUMENTATION PAGE

1. REPORT DATE (DD-MM-YYYY)	2. REPORT TYPE	3. DATES COVERED (From - To)
02/15/2012	Interim Research Performance Report	11/1/2011 - 1/31/2012

4. TITLE AND SUBTITLE
Interim Research Performance Report
Quarterly Report No. 2

5a. CONTRACT NUMBER

5b. GRANT NUMBER
N00014-11-1-0752

5c. PROGRAM ELEMENT NUMBER

6. AUTHOR(S)
Murray, Nathan E.

5d. PROJECT NUMBER

5e. TASK NUMBER

5f. WORK UNIT NUMBER

7. PERFORMING ORGANIZATION NAME(S) AND ADDRESS(ES)
The University of Mississippi
Jamie Whitten National Center for Physical Acoustics
University, MS 38677

8. PERFORMING ORGANIZATION REPORT NUMBER

9. SPONSORING/MONITORING AGENCY NAME(S) AND ADDRESS(ES)
Joseph Doychak
Office of Naval Research
875 North Randolph Street
Arlington, VA 22203-1995

10. SPONSOR/MONITOR'S ACRONYM(S)
ONR

11. SPONSOR/MONITOR'S REPORT NUMBER(S)

12. DISTRIBUTION/AVAILABILITY STATEMENT
Approved for Public Release; Distribution is Unlimited

13. SUPPLEMENTARY NOTES
In collaboration with Charles Tinney (U. of Texas at Austin), Brian Thurow (Auburn Univ.), & Raj Sinha (CRAFT Tech)

14. ABSTRACT

Significant progress has been made on WBS 1.0 and 2.0 items. The MHz PIV system has arrived at NCPA and successfully passed initial system check-out. The near-field microphone array has been built and tested in the UT Austin facility. The specific nozzle hardware to be used for the program has been identified, and mean profile measurements have been completed at the NCPA. CRAFT Tech has completed LES computations of one of the configurations of interest. Graduate students are heavily involved in the activities of each of the academic institutions. The plan for completion of the experimental data collection has been laid out to be completed by the end of the current academic year.

15. SUBJECT TERMS
Jet Noise Reduction

16. SECURITY CLASSIFICATION OF:			17. LIMITATION OF ABSTRACT	18. NUMBER OF PAGES	19a. NAME OF RESPONSIBLE PERSON
a. REPORT	b. ABSTRACT	c. THIS PAGE			Nathan E. Murray
					19b. TELEPHONE NUMBER (Include area code)
				39	662-915-3190

1   Project Objectives and Status

1.1   Objectives Overview

The primary objective for this program is to acquire high-fidelity, time-resolved, synchronous flow-field and acoustic data on a laboratory scale, hot, supersonic, shock-containing jet. The planned experimental campaign includes three nozzle configurations,

- round, conical, converging-diverging (C-D) nozzle,

- round, conical, C-D nozzle with upstream centerbody, and

- faceted C-D nozzle,

each of which will be operated at perfectly expanded ($M_j = 1.74$) and over-expanded ($M_j = 1.55$) conditions at a nominal total temperature of 1350°F. CFD analysis will yield comparative data on these same 6 configurations. These operating conditions were chosen because model hardware already existed from previous NCPA research efforts (funded by ONR and NAVAIR). The nozzle hardware is described in Section 2.1.

1.2   Status of Current and Completed Task Items

The task items for the 'base' program are listed in Table 1 showing the designated team lead and the completion percentage as of the end of the reporting period. The focus of the present work is on WBS 1.0 and 2.0. A brief status of these items is listed here. More detail on the current work is presented in Section 2.

WBS 1.1 This item has been completed; however, the available data from CRAFT Tech on this old simulation only included mean flow information. Currently, time resolved simulations are underway to provide statistical and time-dependent data under WBS 2.3.

WBS 1.2 UT Austin has completed the design and production of the near-field array setup and has completed a check-out experiment in their facility.

WBS 1.3 This task is waiting on time-resolved snap-shots from the CFD which should be completed within the next week.

WBS 1.4 Not yet started. Will use time resolved LES data to begin development.

WBS 2.1 Pressure and select temperature data has been acquired for all configurations. The temperature probe failed. Additional temperature profile measurements will be delayed until a suitable probe fix is completed.

WBS 2.2 The MHz-PIV system has arrived at NCPA from Auburn. Power connections have been made and initial check-out operation of the system has been completed.

WBS 2.3 LES computations for the faceted nozzle without center-body have produced mean and RMS data. Final iterations to produce time-resolved snap-shots are near completion.

WBS	Task	Resource	% Complete
	Main Idea		15
1	Develop Analysis Methodologies and Plan Experiments		39
1.1	Identify Existing LES Data for a Hot Supersonic Jet	CRAFT Tech	100
1.2	Design Near Field Array	UT Austin	100
1.3	Evaluate Expected Jet Velocity Characteristics for PIV Measurements	Auburn	10
1.4	Develop Computation of Space-Time Velocity Correlations	U. Miss NCPA	0
2	Perform Experiments and Computations of a Hot Supersonic Jet		38
2.1	Obtain Single-Point Measurements of Hot, Supersonic Jet Exhaust	Academics	70
2.2	Obtain Synchronous Data for Hot, Supersonic Jets	Adademics	10
2.3	Perform LES Computations of Experimental Conditions	CRAFT Tech	33
3	Analyze and Reduce Experimental Data		
3.1	Reduce and Analyze PIV Data	Auburn Lead	0
3.2	Analyze Near-Field and Far-Field Data	UT Austin Lead	0
3.3	Determine Experimental Uncertainty	U. Miss NCPA Lead	0
3.4	Compute Space-Time Correlations in the Near-Nozzle Region	U. Miss Lead	0
4	Compare Experimental and Computational Results	All	0
5	Acquire Additional Experimental Data (As Needed)	N/A	0
6	Establish Computational Phased-Array Methodology	CRAFT Tech	50
7	Form Conclusions about the Effect of Nozzle Configuration on Noise	All	0
8	Prepare Quarterly Reports	U. Miss NCPA Lead	20
8.1	Q-01 Report		100
8.2	Q-02 Report		100
8.3	Q-03 Report		0
8.4	Q-04 Report		0
8.5	Q-05 Report		0
8.6	Q-06 Report		0
8.7	Q-07 Report		0
8.8	Q-08 Report		0
9	Prepare Final Report	U. Miss NCPA Lead	0
10	Present Results at Annual Review Meetings	U. Miss NCPA Lead	0

Table 1. WBS Listing for Base Program with designated lead team member and completion percentage.
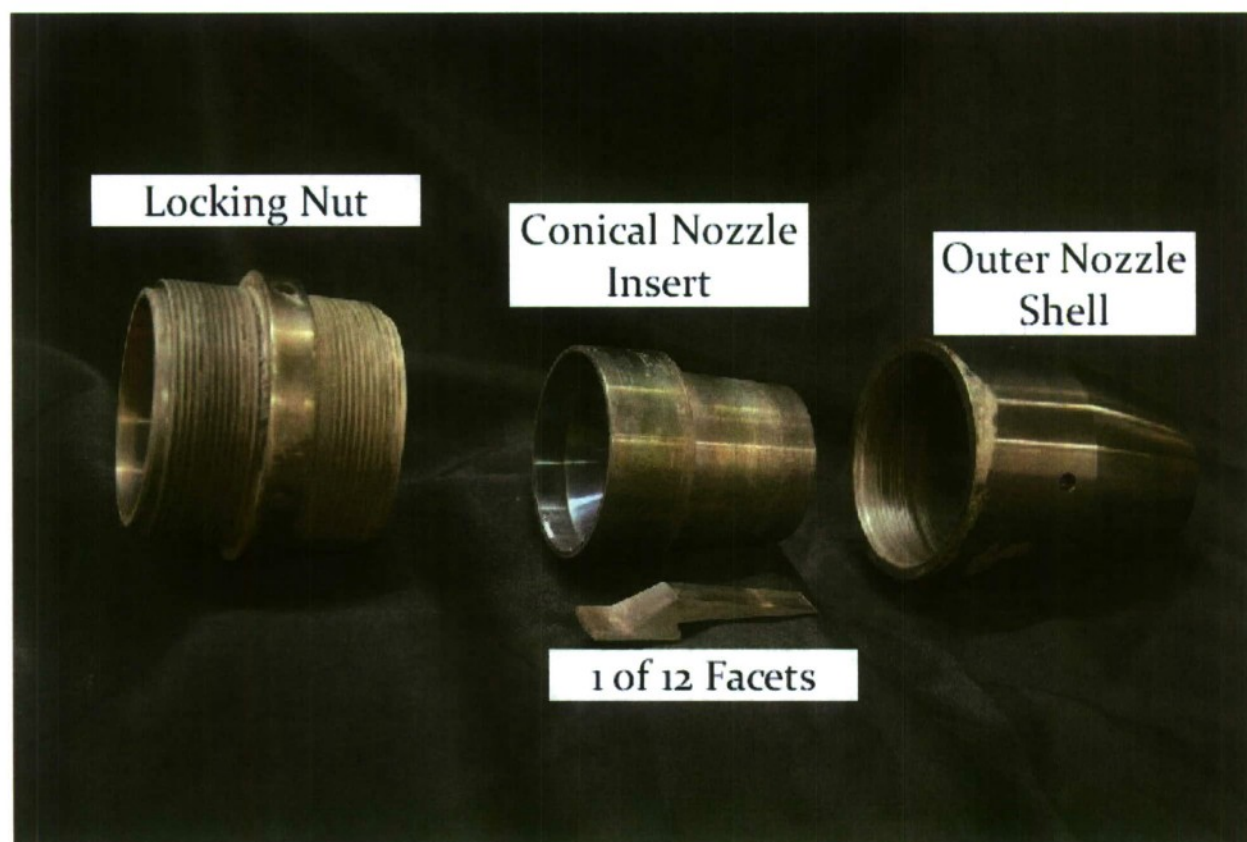
Figure 1. Nozzle assemble showing the outer shell, insert (solid conical and segmented facets), and retaining ring.

2   Activity for Current Reporting Period

2.1   Identification of Nozzle Hardware

Figures 1 through 3 show the model hardware that will be used in the NCPA Anechoic Jet Laboratory (AJL) for the experiments during this program. The model consists of an outer shell with interchangeable inserts held in place by a retaining ring as shown in Figure 1. The conical C-D insert is a single piece while the faceted nozzle is assemble from 12 segments as shown in Figure 2. The centerbody section shown in Figure 3 sits in a 6-inch length of pipe that is replaced with a straight extention when the centerbody is not in use so that the nozzle exit remains in the same position in the test cell.

2.2   Progress on LES Modeling of Hot Supersonic Jets

Following the identification of suitable LES datasets from past programs, CRAFT-Tech initiated new LES calculations for experimental conditions of interest to the current program as outlined in the Statement of Work (WBS 2.3). To date, simulations for the the nozzle using 12 flat facets operated at two pressure conditions, overexpanded and correctly expanded, have been completed. The nozzle operating conditions (stagnation pressure, P_0, stagnation
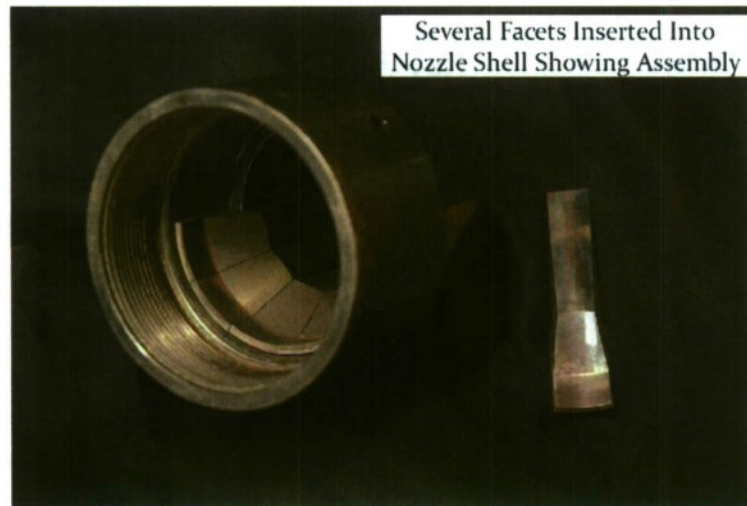
Figure 2. Partially assembled faceted nozzle.

(a) Upstream Side   (b) Downstream Side

Figure 3. Model centerbody used to simulate the spool wake in a full-scale engine.

temperature, T_0, and Mach number, M) are specified in table 2.2. For both nozzle operating conditions, the freestream pressure and temperature were assumed to be $P_\infty = 101.33$ kPa (14.7 psi) and $T_\infty = 300$ K ($\sim$81 ^{0}F) respectively.

	Overexpanded	Correctly Expanded
P_0	401.76 kPa (58.27 psi)	531.33 kPa (77.06 psi)
T_0	1005.4 K (1350 ^{0}F)	1005.4 K (1350 ^{0}F)
M	1.55	1.74

Table 2. Operating conditions for CFD simulations of the faceted nozzle without the centerbody piece.

The calculations were performed using CRAFT Tech's CRAFT CFD® program which is a structured Navier-Stokes solver that uses an upwind differencing scheme that is fifth order accurate in space and a four stage Runge-Kutta algorithm for time marching. The code is highly parallelized using domain decomposition, with close to linear speed-up parallel performance on several large supercomputers for very large grids. To begin, a high-fidelity RANS calculation was performed in order to estimate the flow within the nozzle. Fine wall resolution was included to capture the relatively thin boundary layer at the exit of the nozzle. The solution obtained at the nozzle exit using RANS was used as the inlet condition for the LES calculations. The LES calculations were performed on a grid containing approximately 7 million cells and extended $80R_j$ (R_j is the nozzle radius) in the axial (X) direction and had a radius of $30R_j$ at it's widest extent. Following this, there is a buffer zone that extends a further $40R_j$ in order to damp out unwanted reflection at the LES flow boundaries. Finally, in order to propagate the nearfield acoustics to the farfield, the Ffowcs-Williams and Hawkings (FWH) equation is used. This propagated solution consists of an integration on a fictitious surface surrounding the noise generating mechanisms of the flow. This is achieved by recording the flow variables on this fictitious surface, called the acoustic data surface (ADS), which is located at predetermined constant LES grid levels, with the desired time resolution.

Figures 4 and 5 show contours of the mean flow properties in the streamwise-vertical (X-Z) plane of the jet issuing from the faceted nozzle without the centerbody and operating at overexpanded and correctly expanded conditions respectively. These mean contours clearly show a shock train in the jet plume which is present even when the jet is operated at it's design point (figure 5). This is because the design point is determined using the ratio of the exit area to the throat area. For a shock-free operation, one would require the diverging section of the nozzle to be suitably contoured using the method of characteristics, which is not the case with the faceted nozzle which consists of 12 flat facets in the diverging section (which makes the exit dodecagonal rather than circular). At the overexpanded condition, the pressure at the exit of the nozzle is lower than ambient and the jet adjusts to the freestream by a series of compression and expansion shocks that make up the shock train seen in figure
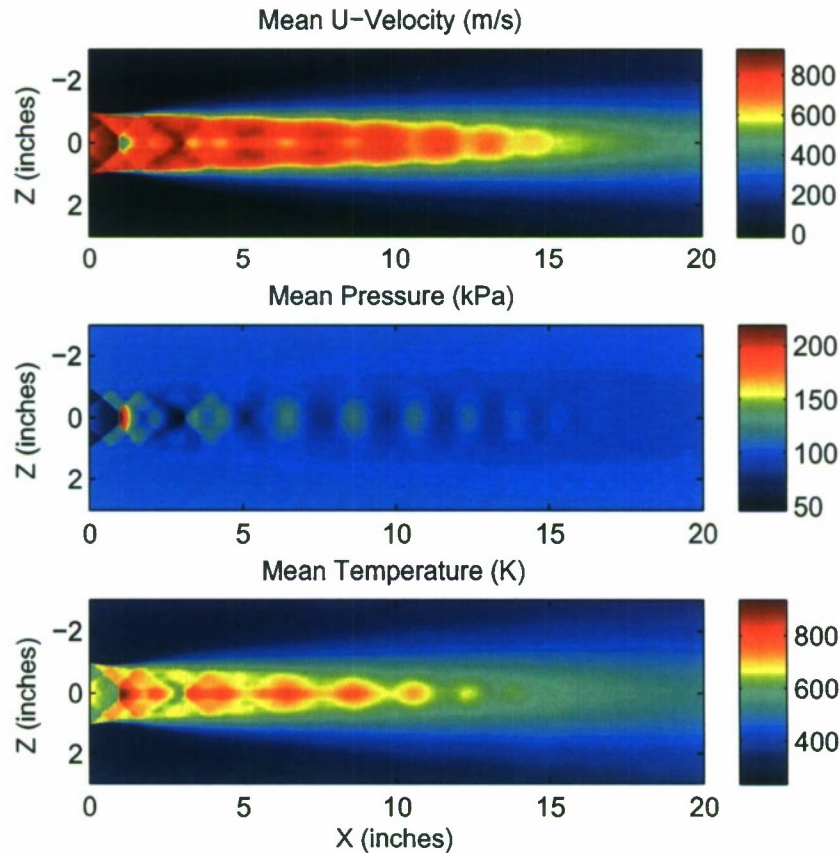
Figure 4. Mean flow quantities in the XZ plane computed by LES for the faceted nozzle without the centerbody operating at overexpanded conditions.

4. Additionally, it is well known that the shock-cell length is directly proportional to the jet Mach number and this can be clearly seen in the figures where the shock-cell length for the correctly expanded jet is larger than that for the overexpanded jet.

Figure 6 shows a comparison of contours of the cross-plane mean streamwise velocity component at various axial locations between the correctly expanded jet and the overexpanded jet. The top contours, at $x = 5$ inches, show that close to the nozzle exit the jet still retains a polygonal shape. This begins blurring rapidly as the jet entrains and mixes with the ambient air and in the middle contours, at $x = 10$ inches, the mean profiles are nearly circular. Finally, in the bottom contours, at $x = 40$, the jets have thoroughly mixed with the ambient to an extent that the core velocity has dropped to less than a third of that at the exit.

Figure 7 compares the fluctuating components of the streamwise velocity for the two jet conditions. For both jets, there is very little fluctuation in the jet core and high fluctuating amplitudes in the shear layer, as seen from the contours on the top row ($x = 5$ inches). As one moves downstream, and the shear layer thickens, the fluctuation amplitudes in the core begin to increase (middle row contours, $x = 20$ inches). Finally, in the bottom row contours
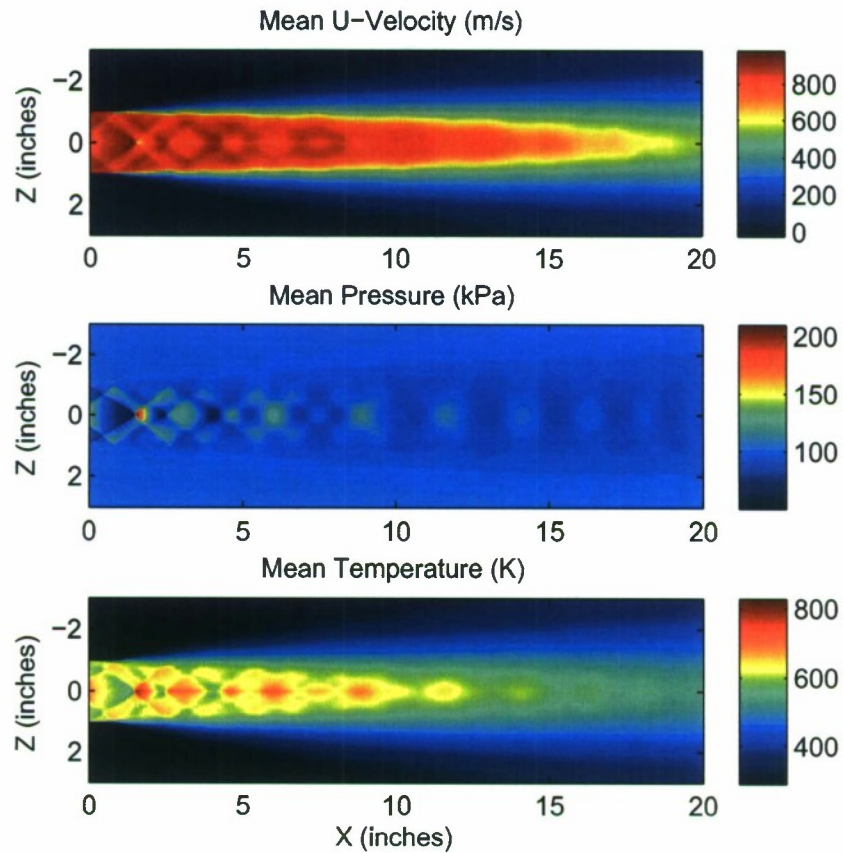
Figure 5. Mean flow quantities in the XZ plane computed by LES for the faceted nozzle without the centerbody operating at correctly expanded conditions.
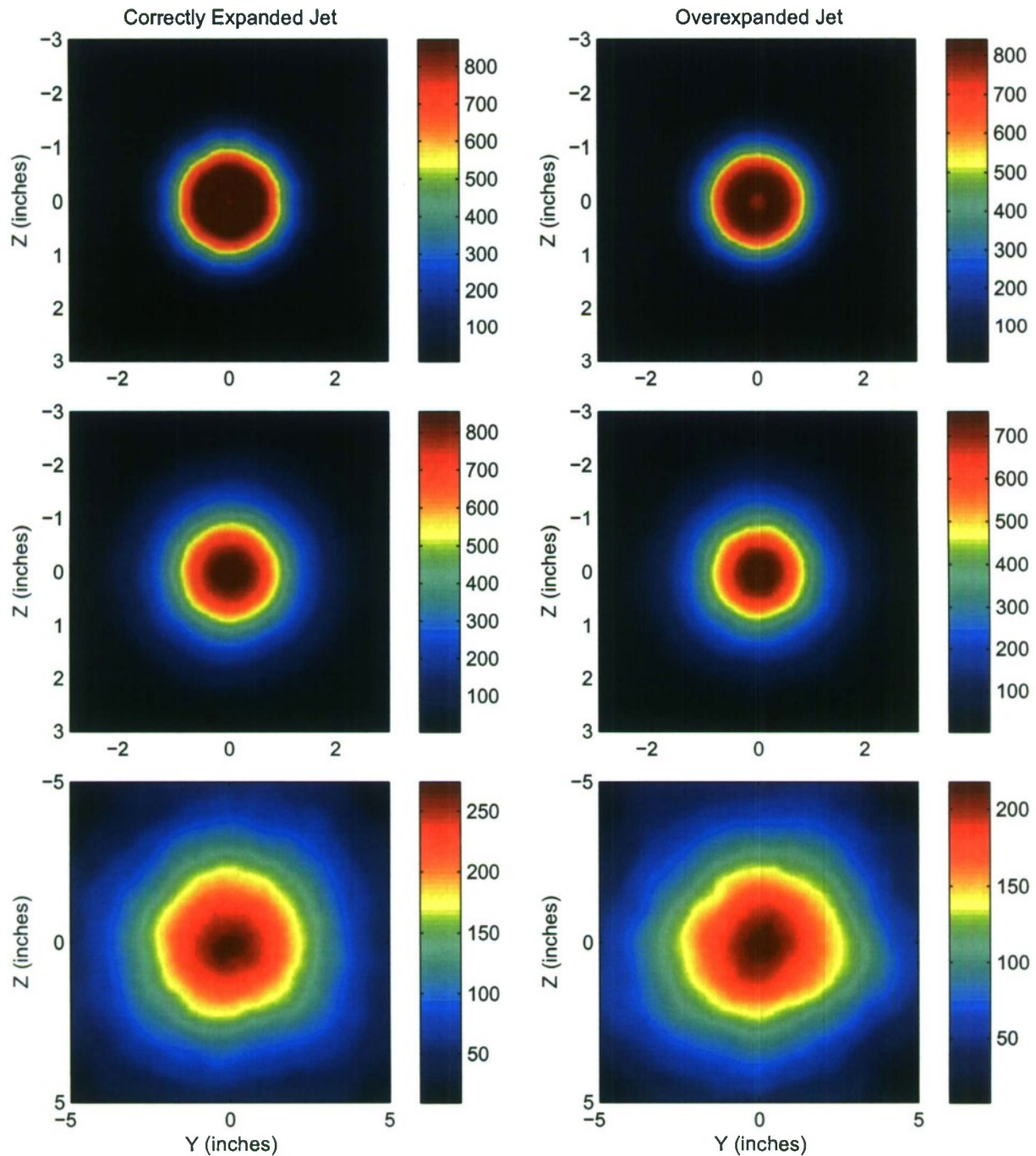
Figure 6. Contours of the mean component of the streamwise velocity in the YZ (cross-) plane computed by LES for the faceted nozzle without the centerbody. Top: $x = 5$ inches, middle: $x = 10$ inches, bottom: $x = 40$ inches.

($x = 40$ inches), well downstream of the potential core, the fluctuations from both jets look similar except for their amplitudes.

Figure 8 shows the decay of the mean streamwise velocity along the centerline axis for the faceted nozzle operating at overexpanded and correctly expanded conditions. The oscillatory nature of the graph at the smaller axial locations indicates the presence and strength of the shock train. Note that even though the correctly expanded jet has higher velocities than the overexpanded jet, the shock oscillations have lower amplitude and damp out faster than those in the overexpanded jet. Assuming the end of the potential core to be located where the streamwise velocity reduces to 50% of the jet exit velocity, the length of the potential core has been determined to be ~ 21.4 inches for the overexpanded jet and ~ 25.4 inches for the correctly expanded jet.

Finally, using the measurements on the gridpoints of the ADS, the spectra at an arc array of microphones located in the farfield can be predicted. These microphones are located 75 equivalent diameters away from the nozzle exit in an arc centered about this exit. The arc consists of 14 microphones located 10 degrees apart starting from 20 degrees measured with reference to the upstream direction. Figure 9 shows the overall sound pressure levels (OASPL) measured by the individual microphones in this array. It is seen that the overall levels peak at 130 degrees in the downstream direction which is in general agreement with jet noise theory.

Future work will involve setting up and performing LES calculations for the straight bore conical nozzle with and without the centerbody in place at overexpanded and correctly expanded conditions, and comparing these calculations to experimental data. Recently, we have obtained access to high performance computing resources with the HPC program which is expected to enhance the speeds at which these LES calculations can be performed.

2.3 Progress on Single-Point Measurements

U. Miss. graduate student, Greg Lyons, has completed single-point profile measurements for all the nozzle configurations of interest. These profiles included total pressure and temperature measurements. Cross-stream profiles were acquired at 4 streamwise stations, and centerline decay profiles were also recorded. The temperature probe proved to be too fragile and failed during testing, so a new probe will be constructed with larger wire diameter and used in future test runs to record this data.

2.3.1 Nozzle Length Correction

Due to the high temperature of the testing, the nozzle grows in the streamwise direction due to thermal expansion. This growth has been observed to be as much as 0.5 inches or $1/4\,D_j$ (the jet diameter $D_j = 2$ inches). This can have a significant impact on the determination of the measurement position. For the profile measurements, a system using a position sensitive detector (PSD) was setup to measure the growth of the nozzle as shown in Figure 10. This method seemed to work suitably except that the high temperature jet exhaust caused significant variance in the PSD output. Therefore, while a nominal correction to the streamwise position was possible, a more robust, deterministic method of tracking the nozzle exit position will be established for future test runs. One potential method is to paint
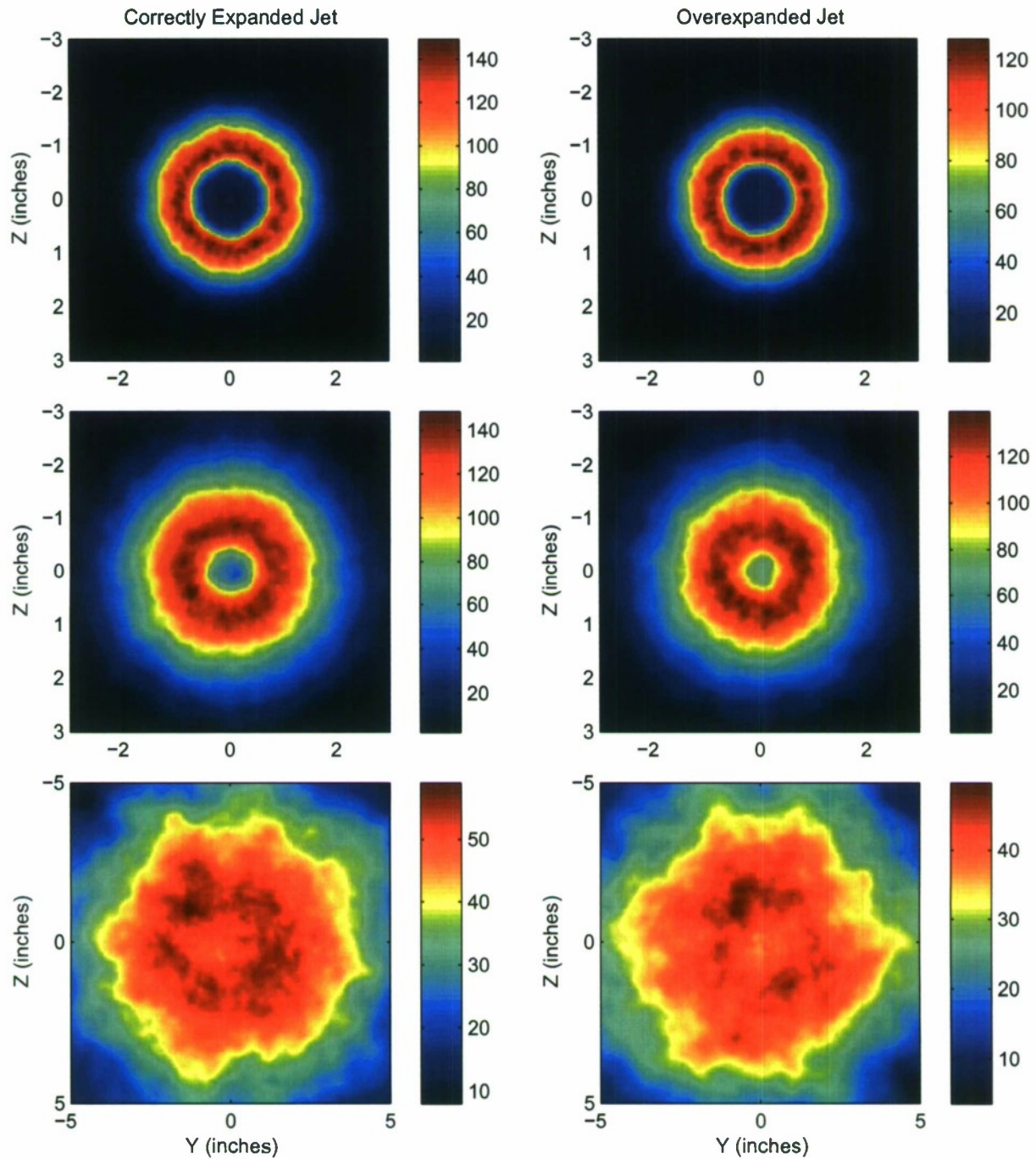
Figure 7. Contours of the fluctuating component streamwise velocity in the YZ (cross-) plane computed by LES for the faceted nozzle without the centerbody. Top: $x = 5$ inches, middle: $x = 10$ inches, bottom: $x = 40$ inches.
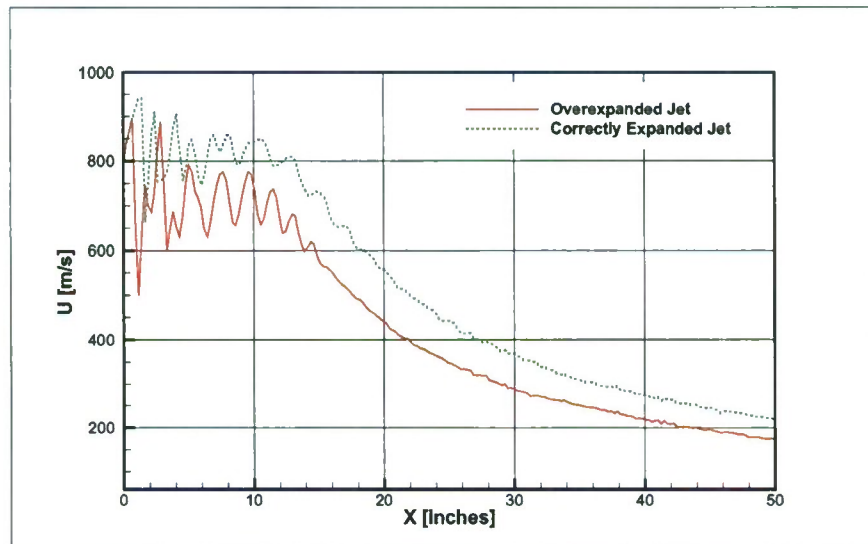
Figure 8. Decay of the mean streamwise velocity in the axial direction along the centerline axis of the faceted nozzle.
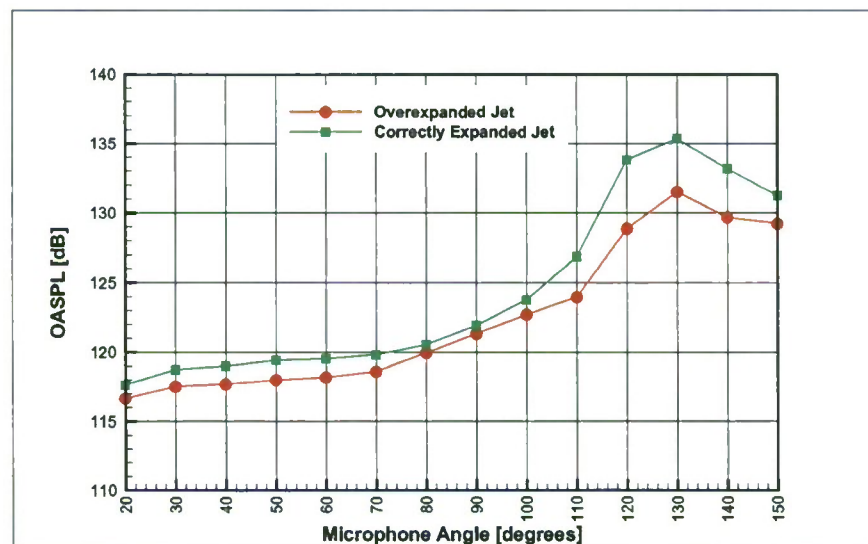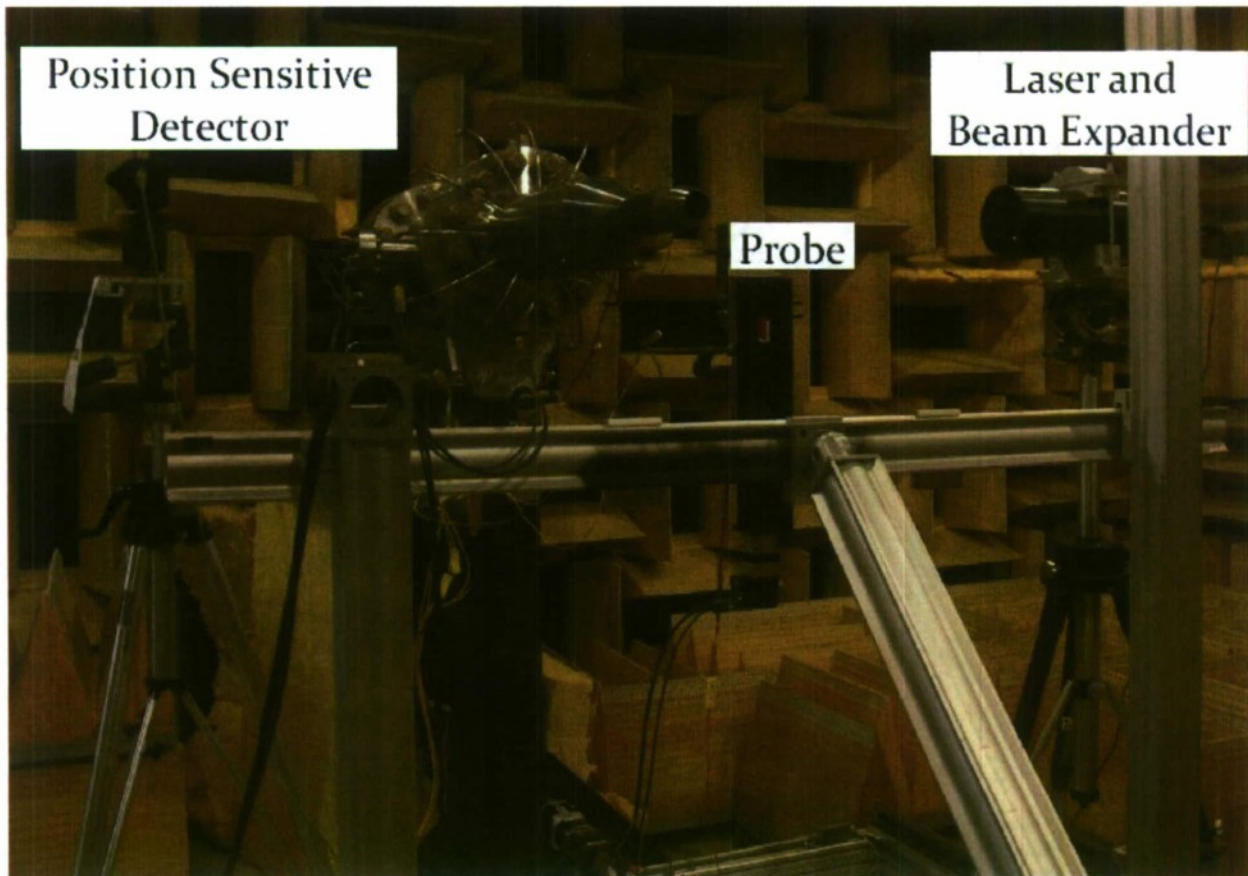

Figure 9. Predicted overall sound pressure levels measured by a farfield array of microphones located 75 nozzle diameters away from the exit.

Figure 10. Probe survey setup for January test runs showing the laser with beam expander and position sensitive detector setup for determining the nozzle exit position during testing.

a tracking dot on the side of the nozzle near the exit and track its position with a digital camera using image calibration to determine the physical growth of the nozzle.

2.3.2 Preliminary Results

Figure 11 shows the profile measurements for the "baseline" (conical C-D nozzle without upstream centerbody) and "cntrbody" (conical C-D nozzle *with* upstream centerbody) configurations at both idealy and over-expanded Mach numbers. It is evident that the centerbody does introduce a slight wake and also creates some asymmetry due to one of the three centerbody supports lining up with the profile plane. The centerbody supports are visible in Figure 3.

Figure 12 shows the centerline survey for each test conditions. The upstream starting location for the first data point in each data set reflects the correction made to the axial position resulting from the thermal expansion of the nozzle. Without this correction, the shock cells for the faceted and baseline nozzles at the overexpanded condition would have appear to be out of phase. However, this should not the case, and the nozzle length correction accurately reflects this in the results presented here. Of special interest is that the simple change from a round to polygonal nozzle shape had a significant effect in the total pressure
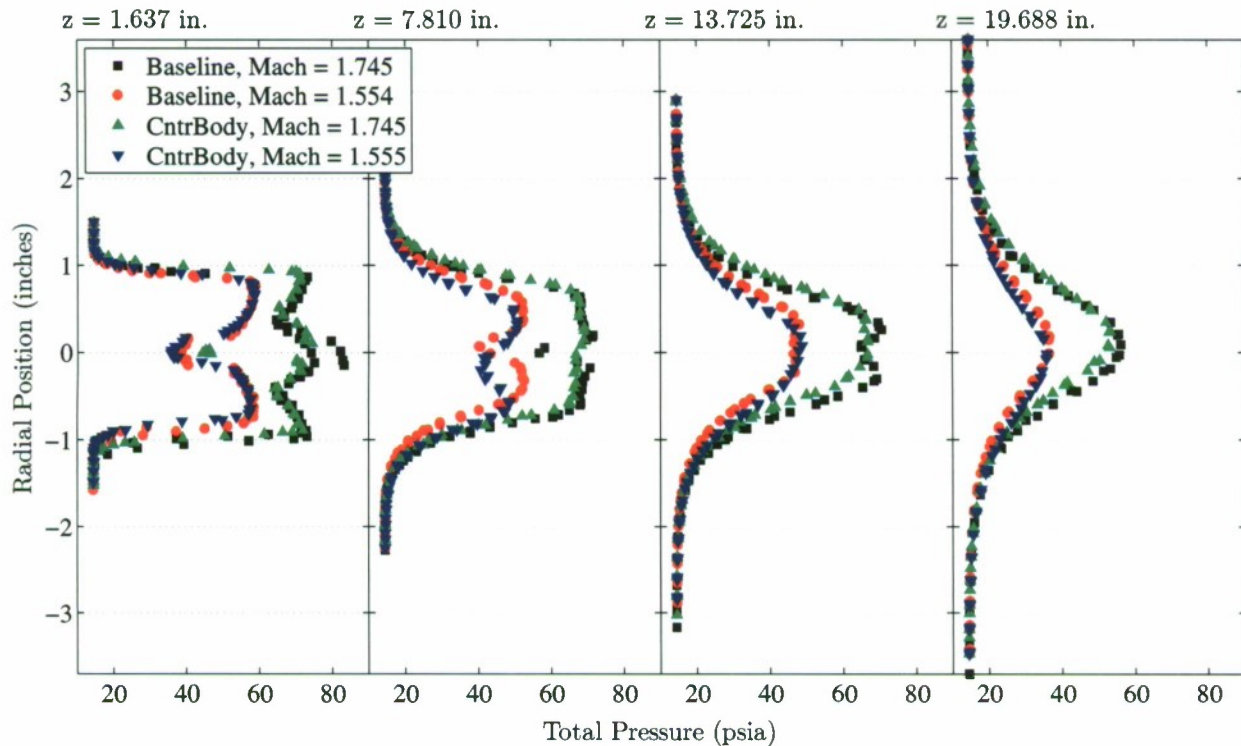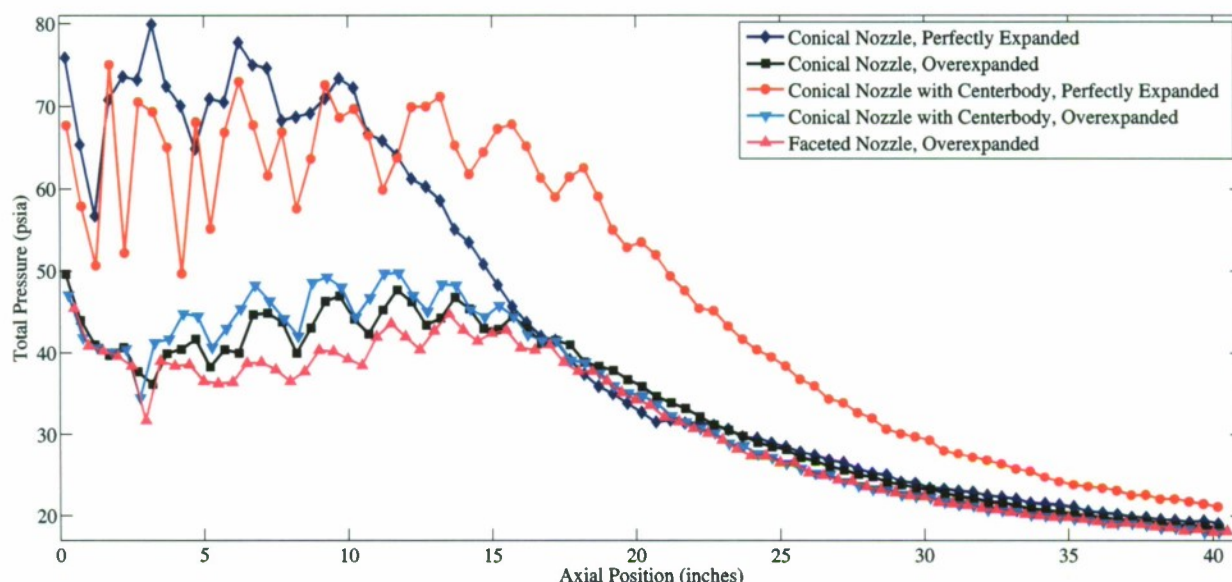
Figure 11. Cross-stream profiles of total pressure for the Baseline conical C-D nozzle and the conical C-D nozzle with upstream center-body ('CntrBody') at both operating conditions. Jet total temperature ~ 1350°.

Figure 12. Centerline total pressure surveys. All data collected at nominal jet total temperature of 1350°.

in the first 5-8 jet diameters. Future data collection and literature research will look for reasons why this may be the case. Another significant observation is that the length of the potential core seems to be dependent on the presence or absence of the centerbody. This effect has been studied in past efforts, and literature research to probe past results will look for support for this result.

2.4 Progress on the Near-Field Acoustic Array

The near-field pressure array had been designed to provide 32 measurement locations along the hydrodynamic periphery of the jet as shown in Figure 13. The U contours shown in the figure are those provided by the CRAFT Tech CFD results.

The array has been built and tested and the Kulite transducers appear to be working acceptably. Figure 14 shows the array in use in the UT Austin facility and a detailed photo of the microphone fixture beam. The length of the array is 48 inches and can be mounted to 8020 rail.

The array was tested using a Mach 3 nozzle (described in Baars, Tinney & Wochner, 2012) at the UT Austin facility. Results of comparing a Kulite transducer (denoted K3 in the figures) with a 1/4″ microphone (denoted M3) mounted in the array are shown in Figures 15 through 17. The Kulites have a slight roll-off at the higher frequencies when compared to the 1/4-inch microphone. After talking with Kulite about this issue, it was determined that this more rapid role off is caused by the tiny vent holes on the Kulite caps which restrict the flow of air in and out of the cavity (chokes the flow in a sense) which then dampens out the higher frequencies. Nevertheless, both are capturing the hydrodynamic hump which is good. Provisions have also been made in the array to attach larger 1/4 inch PCB pressure transducers should a comparison be warrented.
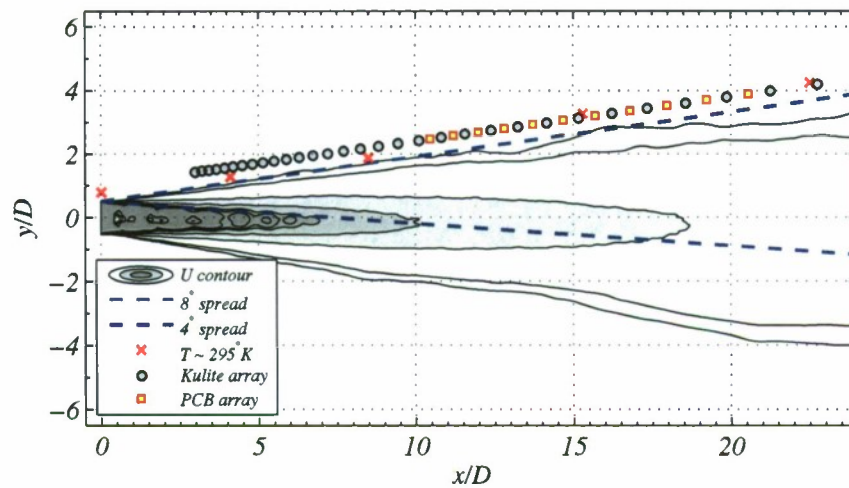
Figure 13. Design of near-field measurement points based on mean flow CFD results.

(a) UT Austin Setup

(b) Near-Field Array Arm
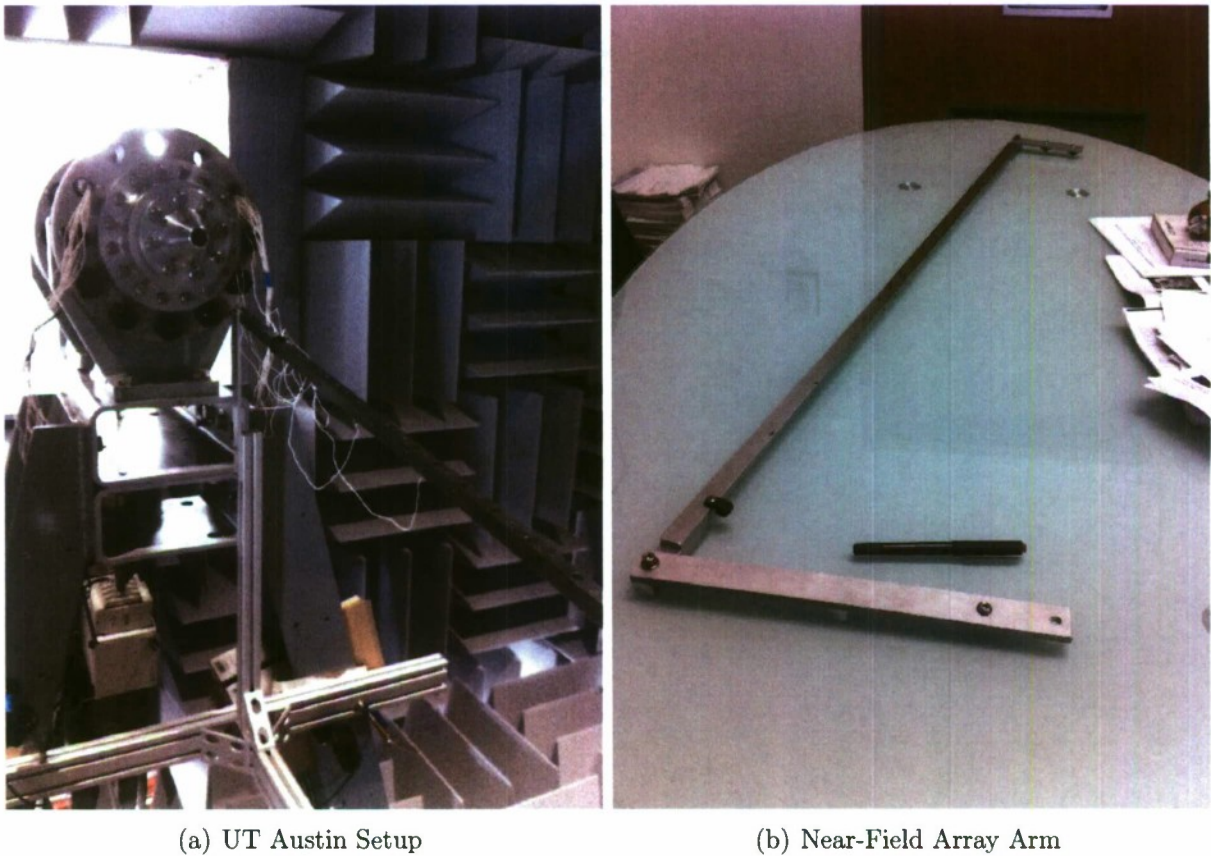
Figure 14. Near-field microphone array apparatus and initial testing in the UT Austin facility.

(a) Spectra

(b) Coherence

Figure 15. Spectra and coherence measured at approximately 2 inch radial distance from $0.1x$ shear layer approximation.

(a) Spectra

(b) Coherence

Figure 16. Spectra and coherence measured at approximately 5 inch radial distance from $0.1x$ shear layer approximation.

(a) Test Run A

(b) Test Run B

Figure 17. Two time traces comparing the Kulite data with microphone data for the near-field array.

(a) Arrival   (b) Unloading

Figure 18. Arrival and unloading of the Auburn MHz PIV system.

The UT Austin graduate student, Brian Donald, plans to arrive at NCPA with the near-field array and related data acquisition hardware on Feb. 20.
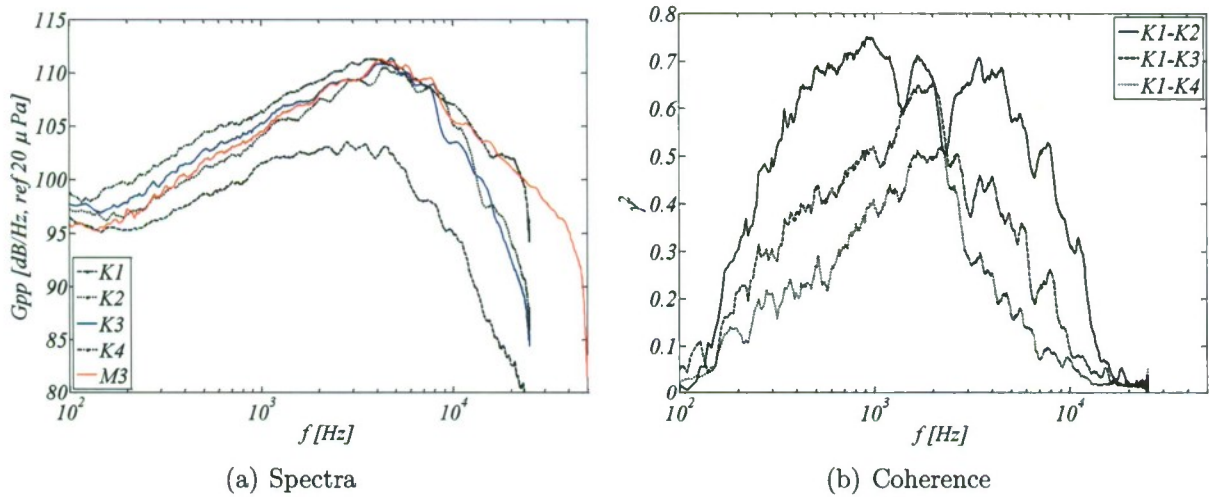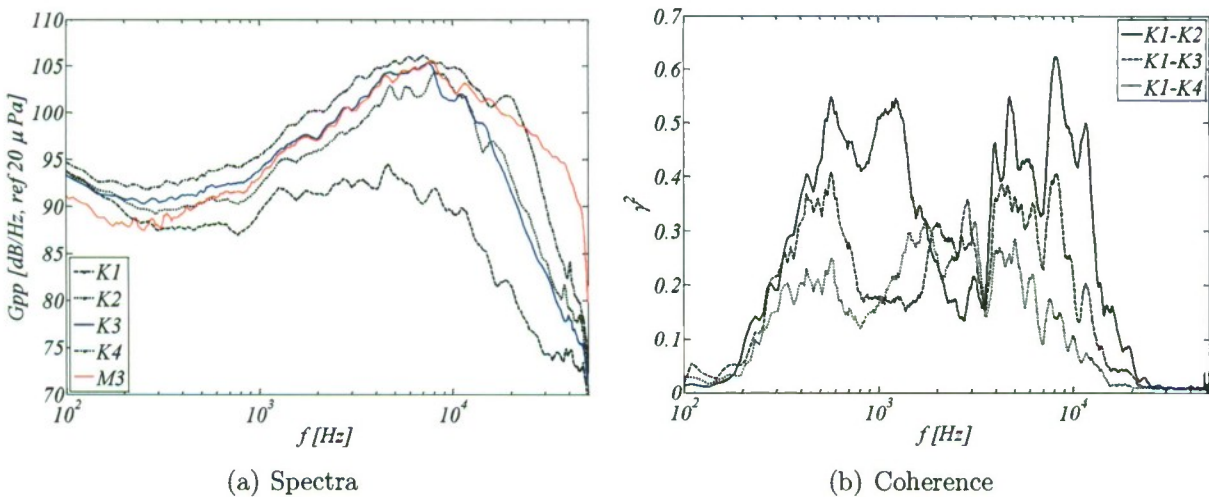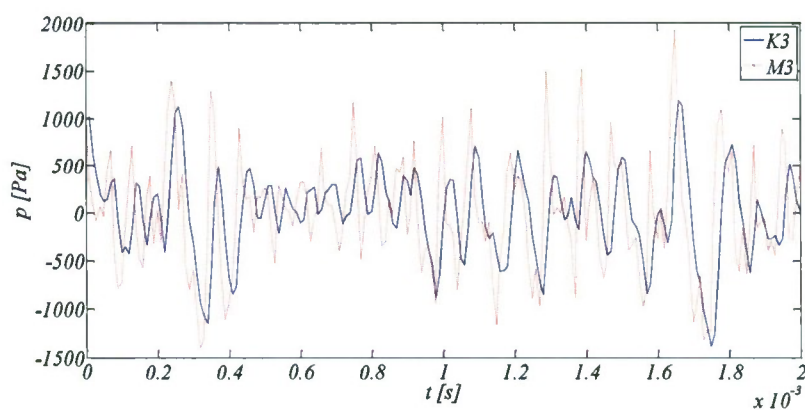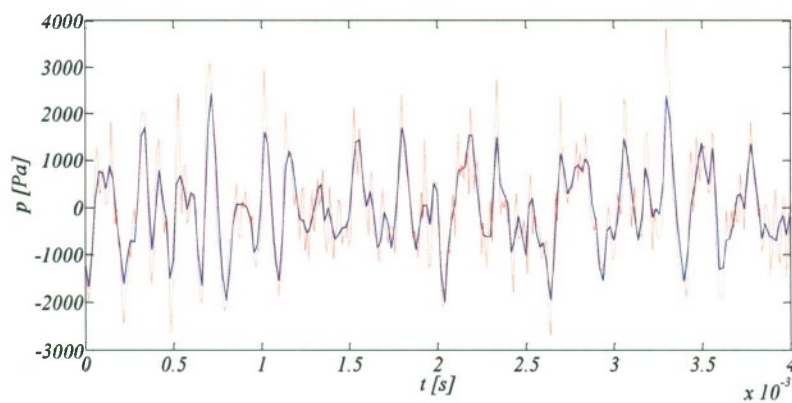
2.5 Progress on MHz-PIV System Setup

The Auburn graduate student, Harris Haynes, arrived safely at the NCPA with the Auburn MHz PIV system. Figure 18 shows the arrival and unpacking of the system. Auburn researchers had taken delivery on the system's new Cordin camera just weeks prior to coming to NCPA and had just received training on the camera's operation. Currently, the power and cooling utilities have been successfully provided to the system and the laser has successfully been operated. Mr. Haynes is current in the process of performing initial check-out image acquisition with the camera to sort out the settings necessary for suitable data collection.

3 Technical/Cost Status & Problem Areas

NCPA received the most recent increment of funds on 20 Jan. 2012 which extends the funded work through 31 March 2012. All technical activities are on schedule.

4 Publications, Meetings, and/or Travel

4.1 Meetings

The PIs from each academic institution met for a planning meeting during the AIAA Aerospace Sciences Meeting held in Nashville, TN, in January. The general planned schedule for the semester was discussed. These plans are presented in Section 5.

4.2 Publications

Full copies of the following publications are also attached as appendices.

[1] Baars, W. J., Tinney, C. E., and Wochner, M. S., "Nonlinear Noise Propagation from a Fully Expanded Mach 3 Jet," In *50th AIAA Aerospace Science Meeting*, Paper AIAA-2012-1177, Nashville, TN, 2012.

ABSTRACT

The high-intensity noise radiated by an unheated and fully expanded Mach 3 jet is investigated experimentally using arrays of microphones placed in the acoustic *near* and *far* farfield of the jet. Under these conditions Mach wave radiation is the most prominent component of turbulent mixing noise in this shock-free supersonic jet. Measurements of the pressure time series are acquired along a grid in the (x, r)-plane in order to quantify the degree of non-linearity in the pressure waveforms. The topography of the OASPL reveal a highly directive sound propagation path emanating from the post-potential core region at $x/D_j = 20$ and along 45° from the jet axis; this coincides with the Mach wave radiation angle that is expected of this flow. Likewise, the spatial growth saturation and decay of the OASPL due to wave steepening is shown to peak around $127D_j$ from the source field identified in the post-potential core region. Various metrics for quantifying the degree of nonlinearity in the acoustic waveforms are computed and include skewness of the pressure derivative, wave steepening factor and the number of zero crossings per unit time. Each metric is shown to produce a slightly unique propagation path, albeit they all follow along similar paths as the OASPL. A second effort focuses on employing an augmented Burgers equation to numerically propagate the temporal waveform at $60D_j$ outward to a distance of $140D_j$ (along the same 45° path coinciding with the maximum OASPL). Both linear and nonlinear forms of the algorithm are employed and include effects of absorption,dispersion and geometrical spreading. Comparison of the predicted and measured waveforms and spectra reveal how the sound radiation is fairly linear over the spatial domain considered in this study.

5 Planned Activities for Next Reporting Period

The next reporting period is expected to see successful operation and data collection by each of the data acquisition systems individually: the acoustic data system and the PIV flow measurement system. The near term plan is to collect near-field and far-field acoustic data on all the test conditions during the two weeks beginning with 19 Feb. Following that effort, the UT Austin group will return to Texas and proceed with acoustic data analysis. In the six following weeks, the focus will turn to optical setup, seeding setup, system checkout,

and data collection with the MHz PIV system. The goal is to acquire data for some of the test conditions by the end of that 6 week period ending on 14 April. At that time, the UT Austin group will return to NCPA on 15 April and the entire research team will focus the following 2 weeks on acquiring synchronized acoustic and PIV data for the test conditions under consideration. This scheduled plan is summarized below:

19 Feb – 3 Mar Acoustic Data System Setup and Data Collection

4 Mar– 14 Apr MHz PIV System Setup, Checkout and Data Collection

15 – 28 Apr Sychronous Acoustic and PIV Data Collection

While these dates remain flexible based on meeting the project objectives, the main goal is to complete this main experimental effort by the end of the academic school year which ends 12 May. This will allow the bulk of the remaining calendar year to be devoted to data analysis and publication.

Appendix A: Baars, Tinney & Wachner (2012) AIAA-2012-1177

Nonlinear Noise Propagation from a Fully Expanded Mach 3 Jet

Woutijn J. Baars* and Charles E. Tinney†

Aerospace Eng. and Eng. Mechanics, The University of Texas at Austin, Austin, TX 78712, USA

Mark S. Wochner‡

Applied Research Laboratories, The University of Texas at Austin, Austin, TX 78713, USA

The high-intensity noise radiated by an unheated and fully expanded Mach 3 jet is investigated experimentally using arrays of microphones placed in the acoustic *near* and *far* far–field of the jet. Under these conditions Mach wave radiation is the most prominent component of turbulent mixing noise in this shock-free supersonic jet. Measurements of the pressure time series are acquired along a grid in the (x, r)-plane in order to quantify the degree of non-linearity in the pressure waveforms. The topography of the OASPL reveal a highly directive sound propagation path emanating from the post-potential core region at $x/D_j = 20$ and along 45° from the jet axis; this coincides with the Mach wave radiation angle that is expected of this flow. Likewise, the spatial growth saturation and decay of the OASPL due to wave steepening is shown to peak around $127D_j$ from the source field identified in the post-potential core region. Various metrics for quantifying the degree of nonlinearity in the acoustic waveforms are computed and include skewness of the pressure derivative, wave steepening factor and the number of zero crossings per unit time. Each metric is shown to produce a slightly unique propagation path, albeit they all follow along similar paths as the OASPL. A second effort focuses on employing an augmented Burgers equation to numerically propagate the temporal waveform at $60D_j$ outward to a distance of $140D_j$ (along the same 45° path coinciding with the maximum OASPL). Both linear and nonlinear forms of the algorithm are employed and include effects of absorption, dispersion and geometrical spreading. Comparison of the predicted and measured waveforms and spectra reveal how the sound radiation is fairly linear over the spatial domain considered in this study.

I. Introduction

To date, there continues to be a lack of consensus in the scientific community regarding the precise mechanisms by which sound, generated by jet flows, propagates to an observer far from the flow. For high supersonic Mach number jets, the problem is further exacerbated by the fact that highly directive and intense noise patterns –produced by the formation of Mach waves– undergoes nonlinear wave steepening and coupling along the propagation path and has proven difficult to model. To some relief it is well agreed upon that the sound generated by supersonic jets comprises three distinct mechanisms: turbulent mixing noise, broadband shock-associated noise and screech tones. The latter two manifest themselves when shock structures are present in the plume. The current work focusses on characterizing the non-linear behavior of the turbulent mixing noise produced by a cold, fully expanded, Mach 3 jet. The test article under investigation comprises a Method of Characteristics contour thus eliminating the sources of noise associated with shock cells and screech.

It has been postulated for quite some time that turbulent mixing noise consists of two components. The first component is generated by large turbulent structures or instability waves that pass along the potential core regions of the flow whereas the second component is believed to be associated with the fine-scale turbulence within the shear layer and is omni directional.[1] Where the large-scale structures are concerned,

---

*PhD Candidate, AIAA Student Member.
†Assistant Professor, AIAA Senior Member. http://www.ae.utexas.edu/facultysites/tinney/
‡Research Associate.

these events act as surface panels convecting at supersonic speeds that radiate waves at the Mach cone half angle: $\phi = \pi/2 - \mu = \pi/2 - sin^{-1}(a_\infty/U_c)$ as shown in figure 1. This process forms within the zone of action and becomes increasingly intense as the convective Mach number of the turbulent large-scale structures travel at supersonic speeds relative to the ambient. Between the zone of action and zone of silence, the intensity of these radiating waves rapidly decays. The process of Mach wave radiation is highly complex and has been the subject of numerous investigations.[2-6] The complexity of this problem is attributed to various factors including 1.) growth, saturation and decay of the instability waves along the jet axis, 2.) the non-uniform and frequency dependent convective speeds of the large scale structures, and 3.) additional factors such as acoustic refraction in the case of non-isothermal jets.
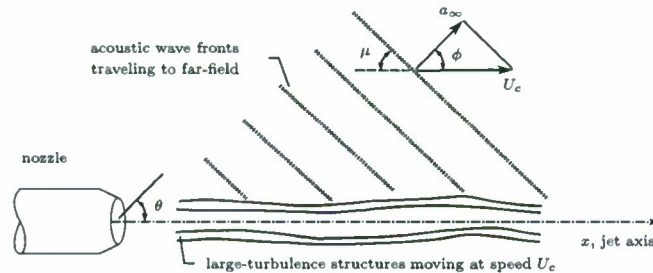

Figure 1. Simplified schematic of the Mach wave radiation mechanism in the near-field of the jet (ambient speed of sound a_∞ and uniform convective speed U_c of the instability waves).

A wide variety of experimental and numerical studies have been conducted in the past on supersonic jets. Contributions from the 1970's on include the work by McLaughlin *et al.* (1975),[2] Tanna & Dean (1975),[7] Morris (1977),[8] Troutt & McLaughlin (1982),[9] Crighton & Bashforth (1980),[10] Gallagher (1982),[11] Tam *et al.* (1992)[12] and Seiner *et al.* (1994).[3] More recent investigations include the work by Bridges (2006)[13] and Bridges & Wernet (2007)[14] of supersonic jets based on the gas dynamic Mach number and McLaughlin *et al.* (2010)[15] and Baars *et al.* (2011)[16] of supersonic jets based on the acoustic Mach number. Where the development of more robust and accurate acoustic analogies are concerned, one may wish to review the work of Tam *et al.* (2008)[5,6] and Morris (2009).[17] While a great number of these surveys have focused on noise from supersonic jets in general, very few have attempted to investigate the nonlinear propagation that is solely associated with the high-intensity turbulent mixing noise. Even fewer studies have focused on the time series waveforms of the acoustic pressure in the far-field of the flow that form along the dominant propagation path within the cone of action. Regarding the last topic, the reader is referred to the work by Gallagher (1982),[11] Petitjean *et al.* (2006)[18] and Gee *et al.* (2008).[19]

Where nonlinear acoustics are concerned, it is well known that waveforms produced by high-intensity sources are subject to change shape due to wave steepening, shock formation, viscous/atmospheric absorption, shock coalescence and relaxation phenomena. This distortion is illustrated in figure 2a for an initial sinusoidal waveform and is well explained in the literature on nonlinear acoustics.[20,21]

Groundbreaking work by Pestorius and Blackstock (1973)[20] resulted in the development of methods capable of applying nonlinear acoustic theory to broadband signals. The study focussed on the propagation of a broadband noise pulse emitted by a high-intensity source in an air-filled progressive wave tube. Excellent agreement was achieved between the measured and computed waveforms at various locations downstream of the source. It was the first introduction of an algorithm capable of propagating arbitrarily shaped waveforms in one dimension while incorporating shock formation and relaxation effects. During the nonlinear propagation of broadband signals, wave steepening and shock formation effects distort the waveform during its infancy stages which become more pronounced with outward distance from the source. This results in a transfer of energy from the mid frequency range to the high frequency end of the spectrum. In addition, strong shocks travel faster than weak shocks in the waveform. And so, shocks coalesce which is manifested by a decrease of zero crossings in the waveform associated with a shift of energy from the mid frequencies to the low frequencies. Thus, if viscous absorption permits, nonlinear effects results in an overall broadening of the spectrum.

In high-speed jet flows, a variety of different approaches have been considered for dealing with the nonlinear propagation phenomena. A common method for obtaining scaled *far* far-field pressure spectra is to project a power spectral density function obtained in the *near* far-field and then apply corrections
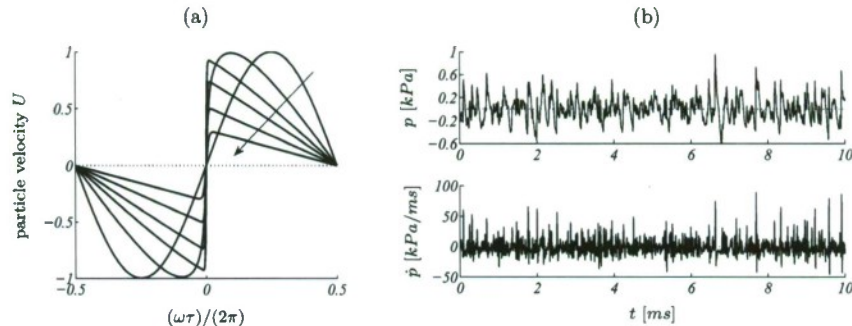
Figure 2. (a) Schematic of the distortion of a sinusoidal waveform during nonlinear propagation including the effect of viscous absorption, (b) Measured acoustic waveform of broadband jet noise indicating evidence of nonlinear effects *(top)* and the time derivative of the pressure waveform *(bottom)*.

for atmospheric absorption followed by spherical spreading. Any differences between the measured and predicted *far* far-field spectra are then attributed to nonlinear distortion. Howell & Morfey (1987)[22] derived a nonlinear indicator as a means by which one could quantify this degree of nonlinearity. In essence, this indicator is a measure of how the energy in the power spectral density is redistributed due to nonlinear effects. Applications of the Howell & Morfey (1987) indicator to problems in jet noise can be found in the literature.[18, 23, 24]

Another approach to study nonlinear propagation is based on a correlation study between near-field and far-field data using higher-order spectral analysis methods. Originally developed by the systems identification community, these techniques are designed to quantify nonlinear coupling in a single-input/output system. These bispectral methods identify nonlinearities by computing the quadratic bicoherence, which is essentially the second-order variant of the well-known linear coherence. By applying these techniques one can essentially identify the frequencies at which two signals are linearly and nonlinearly related.[23, 25] Since the bispectral technique is an identification technique and does not provide the direct capability of estimation and prediction. another technique developed in the field of system identification was introduced which started with the work of Tick (1961).[26] This higher-order estimation technique is presented in the recent work of Baars, Tinney & Powers (2010)[27] where it is combined with proper orthogonal decomposition to allow the application of this technique to sets of sensors in the near-field and far-field, thereby eliminating the limitation of single-sensor analysis. It is a promising technique but due to current practical limitations the technique is confined to second order (quadratic) systems and low frequency resolution. A second difficulty arises due to convergence issues of higher-order spectral moments which casts doubts on one's ability to reveal the true nature by which the nonlinear distortion is manifest.

I.A. Overview of current study

In the present work, a grid of microphones placed in the *near* and *far* far-field along a slice in the (x, r)-plane of a Mach 3 jet are used to acquire the temporal acoustic waveform in order to gauge the degree of acoustic nonlinearity produced by this type of jet flow. This Mach number is not typical of commercial or military aircraft engines and so bears little relevance to practical systems of engineering interest. However, the high Mach number does ensure the formation of strong Mach waves which can provide insightful information into the nonlinear propagation phenomenon observed in lower supersonic Mach number jet flows. A sample temporal waveform from this study is shown in figure 2b which demonstrates the wave steepening effect expected from this type of nozzle. Included below this illustration is the temporal derivative which demonstrates the expectation of a non-zero skewness.

As a first approach to characterizing the degree of nonlinearity in the pressure waveforms captured along this (x, r) grid, the following metrics are considered:

- ***Skewness of the pressure derivative.*** The amount of wave steepening, and thus the nonlinearity

American Institute of Aeronautics and Astronautics

in the pressure signal, can be quantified by computing the probability density function (PDF) and skewness factor of the pressure time derivative $\dot{p}(t)$. The PDF is denoted as $B(\dot{p})$. The asymmetry of the PDF can be quantified by the third central moment, defined by[28]

$$\overline{\dot{p}^3} \equiv \int_{-\infty}^{\infty} \dot{p}^3 B(\dot{p}) \, d\dot{p}. \tag{1}$$

A dimensionless measure of this asymmetry is the well known *skewness* factor, and is defined as

$$S \equiv \frac{\overline{\dot{p}^3}}{\sigma^3}, \text{ where } \sigma \text{ is the variance of } \dot{p}(t). \tag{2}$$

- **Wave Steepening Factor.** The wave steepening factor (WSF) is defined as the modulus of the average negative slope divided by the average positive slope in the waveform.[11] The range of WSF is thus $[0, 1]$, where 1 corresponds to a pure harmonic wave and 0 to a perfect N wave.

- **Zero crossings per unit time.** Since stronger shock waves move faster in the waveform and merge or coalesce with weaker shocks, the number of zero crossings of the waveform $p(t)$ will change. When shocks coalesce, a decrease in zero crossings, Z_c, appears with propagation distance and is therefore a measure of nonlinearity.

A second effort focuses on application of a hybrid time-frequency domain algorithm that numerically solves the generalized Burgers equation using an input waveform from a *near* far-field acoustic microphone at $60D_j$ to predict its waveform at $140D_j$ (along the same 45° path coinciding with the maximum OASPL). The predicted waveform at $140D_j$ is compared to the simultaneously measured waveform (accounting for phase lags in time) and is analyzed using both linear and nonlinear methods. This hybrid Burgers equation takes into account atmospheric absorption, molecular relaxation losses, nonlinearities, dispersion, and geometrical spreading and is written as follows:

$$\frac{\partial p}{\partial r} = \frac{\beta}{2\rho_0 c_0^3} \frac{\partial p^2}{\partial \tau} + \psi_\tau \{p\} - \frac{1}{r} p, \tag{3}$$

where p is acoustic pressure, r is the range between the first and second observer locations, β is the coefficient of nonlinearity (equal to 1.201), ρ_0 is ambient density, c_0 is ambient sound speed, τ is retarded time, and ψ_τ is the atmospheric absorption and dispersion operator. The algorithm is based on the work of Pestorius and Blackstock (1973)[20] which has been applied more recently to problems in jet noise by Gee *et al.* (2008).[19] The algorithm propagates input time waveforms in a stepwise manner by first applying a nonlinear distortion step using the Earnshaw[21] solution. Absorption, dispersion, and geometrical spreading losses are then accounted for in the frequency domain. Given sufficiently small spatial steps, in this case 1/10 of a shock formation distance, the time and frequency domain steps can be treated independently. In addition, the algorithm can be formulated to perform both linear and nonlinear predictions of the input waveform. For linear predictions, the first term on the right hand side of Eq. (3) is removed, thus allowing the propagation of the waveform between the first and second observation points to be fully calculated in the frequency domain and in one simple step.

II. Experimental Arrangement

II.A. Experimental Facility

The experimental study was performed in the anechoic chamber located on the J.J. Pickle Research Campus of The University of Texas at Austin. The fully anechoic chamber has internal dimensions (wedge tip to wedge tip) of 18ft.(L)×14ft.(W)×12ft.(H). The melamine wedges, in combination with the design of the ceiling and walls, provide a normal incidence sound absorption coefficient of 99% for frequencies above $100Hz$. The chamber allows entrained flow to enter through a $4ft \times 4ft$ opening behind the nozzle jet rig which then exhausts through a $6ft \times 6ft$ acoustically treated eductor on the opposing wall. The nozzle, wind tunnel inlet and wind tunnel eductor are all positioned along the centerline of the chamber.

A custom fabricated nozzle test rig allows different nozzle configurations to be tested and is shown in figures 3 and 4. The rig comprises various hardware components (figure 4a), including a National Instruments
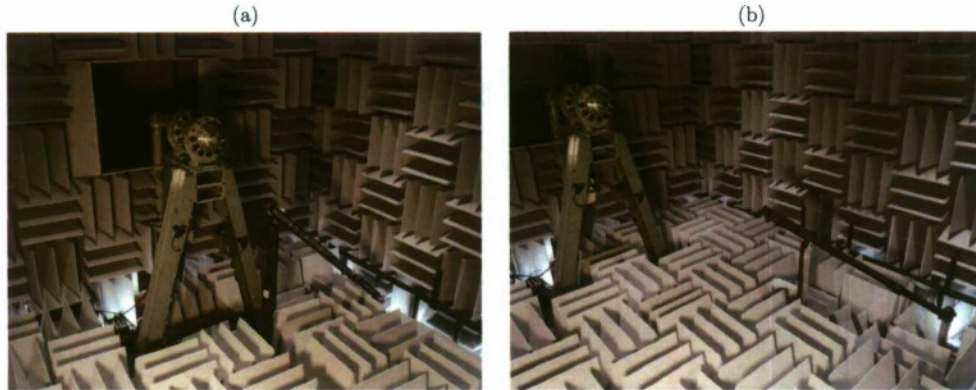
Figure 3. Arrangement of the chamber, nozzle test rig, and microphone array during (a) the grid measurements and (b) the line-array measurements.

(NI) CompactRIO system for operating the control valve upstream of the nozzle. Several instruments are used to monitor and record the nozzle operating conditions and comprise: atmospheric chamber pressure (p_∞), total pressure (p_0) and total temperature (T_0) of the supply air, and the storage tank pressure. The nozzle jet rig and storage tanks are connected by a high-pressure 4in carbon steel pipeline capable of transporting dry compressed air up to 2,100psi (143atm) according to ASME standards. Storage tanks located in a separate building provide 140ft^3 $(4.25m^3)$ of total water volume storage. Leading up to the nozzle test rig is a $4in$ carbon steel line connected to a 6in inner diameter settling chamber. This settling chamber is located immediately upstream of the nozzle mounting flange and houses a Corning Celcor, ceramic flow straightener (400 square cells per in^2 substrate) to condition the flow before entering into the nozzle contraction.
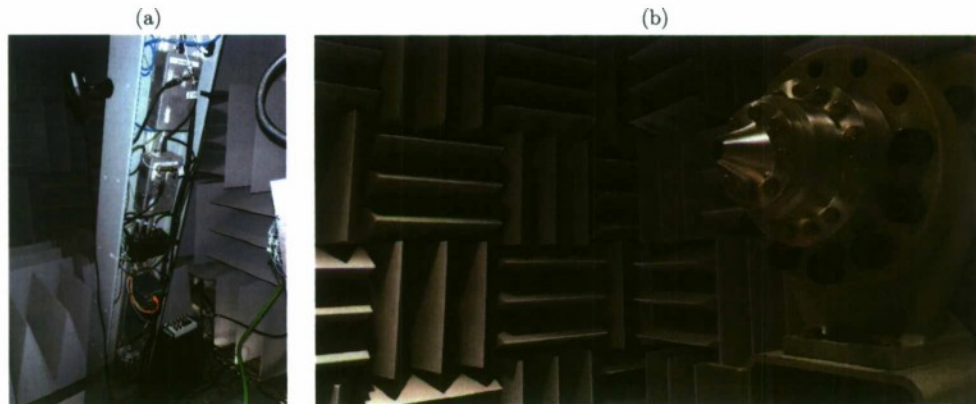

Figure 4. (a) Close-up of the hardware mounted to the nozzle test rig, (b) The Mach 3 MOC nozzle, and additional contraction part, mounted to the settling chamber.

For the present study, a nozzle with an exit gas dynamic Mach number of M_e =3.00 (ambient total temperature, T_0 =273.15K, ratio of specific heats, γ =1.4, specific gas constant of air, R = 287.05J/kg/K) was designed using the Method of Characteristics and fabricated by in house technicians. The nozzle has an exit diameter of 1in (25.4mm) and is 2.30in in length (throat–exit). The nozzle was operated at a nozzle pressure ratio $(NPR = p_0/p_\infty)$ of 36.73 during all runs to achieve a fully expanded, shock-free flow. The

associated mass flow was computed to be 1.04kg/s. The convergent-divergent nozzle piece was attached to an additional contraction (6in to 2in diameter) which was mounted to the settling chamber as is shown in figure 4b.

II.B. Instrumentation and Microphone Arrangement

Acoustic data was acquired using four 1/4in prepolarized, pressure-field, condenser microphones (PCB, model 377B10 and matching preamplifiers model 426B03). The microphones have a frequency response range of 4Hz to 70kHz with ± 1 dB error up to 20kHz and a dynamic range of up to 170dB (re 20μPa). A NI-PXI-1042Q system (low 43dBA acoustic emission) with an eight channel NI PXI-4472 module provided the necessary IEPE conditioned power (27VDC and 4mA) to operate the microphones all the while conditioning the input signal to eliminate aliasing prior to digitization. All four channels were acquire synchronously at a rate of 102.4kS/s with 24bit resolution for a minimum of 2^{20} samples. The microphones were connected by 85ft length cables to the data acquisition system located in a separate control room. It is also important to point out that all measurements were performed with the microphone diaphragms oriented at grazing incidence to the acoustic wave front (plane of the diaphragm intersects with the complete jet axis) and with the microphone grid caps removed.

Two different microphone configurations were used to capture the *near* and *far* far-field acoustic data for this study. These comprised a dense two-dimensional grid aligned perpendicular to the jet axis and a line array positioned strategically along the Mach cone half angle of the jet and are shown in figures 5a and 5b, respectively. These two configurations are described in more detail as follows.
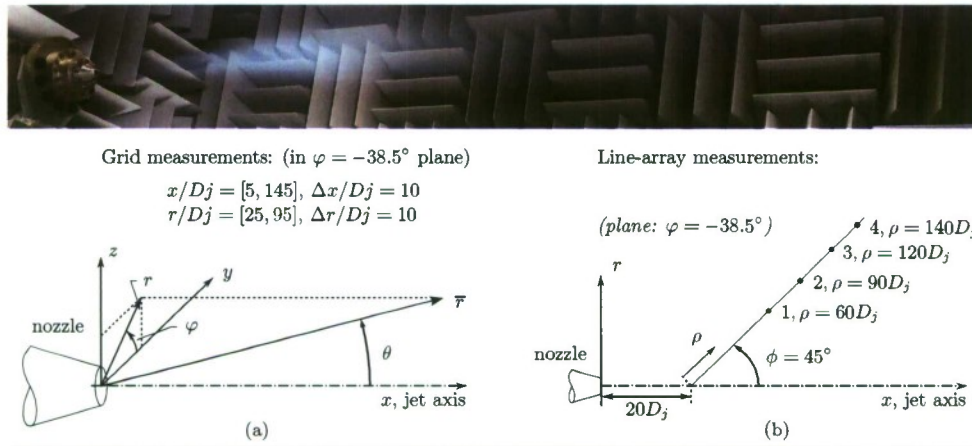

Grid measurements: (in $\varphi = -38.5°$ plane)

$x/Dj = [5, 145]$, $\Delta x/Dj = 10$
$r/Dj = [25, 95]$, $\Delta r/Dj = 10$

Line-array measurements:

(plane: $\varphi = -38.5°$)

4, $\rho = 140 D_j$
3, $\rho = 120 D_j$
2, $\rho = 90 D_j$
1, $\rho = 60 D_j$

$\phi = 45°$

$20 D_j$

Figure 5. *(top)* Visibility of the Mach 3 plume during a run with high relative humidity. (a), coordinate system of the nozzle and arrangement of the grid measurements, (b) schematic of the microphone line-array setup.

- *Planar grid measurements.* A planar two-dimensional grid was constructed in the (x, r)-plane at an angle $\varphi = -38.5°$ relative to the chamber floor. The grid spanned from $5D_j$ to $145D_j$ in the axial direction and from $25D_j$ to $95D_j$ in the radial direction with uniform spacings of $\Delta x = \Delta r = 10D_j$. The furthest microphone position was located at $|\overline{r}| = 173.3D_j$ and $\theta = 33.2°$. An illustration of this during one of the tests is shown in figure 3a. For the purposes of comparing results to others found in the open literature an 'artificial' arc-array at $\rho = 100D_j \pm 1.5\%$ was created by selecting microphone positions listed in table 1.

- *Line-array measurements.* After processing the planar grid measurements, the sound propagation path could be determined and was found to emanate from the post-potential core region at $x/D_j = 20$ and along 45° from the jet axis. This allowed the single line-array of four microphones to be installed and positioned so as to follow the Mach cone half angle of $\phi = 45°$ and with an intersection at

$x = 20D_j$. The microphones were positioned at $\rho/D_j = 60, 90, 120$ & 140 along the array. Considering the motivation for the placement of this line-array, the Mach cone half angle (Mach wave radiation angle) for this nozzle is around $\phi = 45°$.

Table 1. Selection of eight microphones for the 'artificial' arc-array.

mic #	1	2	3	4	5	6	7	8
$(x, r)/D_j$	(115,25)	(115,35)	(105,55)	(95,65)	(85,75)	(75,85)	(55,95)	(45,95)
$\phi\ [degr]$	14.7	20.2	32.9	40.9	49.1	57.1	69.8	75.3
ρ/D_j	98.2	101.2	101.2	99.3	99.3	101.2	101.2	98.3

II.C. Experimental Conditions

Experiments were conducted over a duration of three days during fall time conditions in Austin, Texas. Rare weather conditions produced high humidity levels for the first (75%) and second (63%) days of testing which eventually dropped to 48% by the third day. These environmental conditions were monitored and recorded periodically throughout the duration of the experiments and are listed in table 2. Condition 'grid-array *(day 1)*' corresponds to the measurements performed using the grid-array located at: $x/Dj = [5, 95]$, $r/Dj = [25, 95]$, whereas condition '*(day 2)*' pertains to the remaining sections of the planar grid: $x/Dj = [105, 145]$, $r/Dj = [25, 95]$. For all conditions the nozzle was operated at fully expanded conditions, thus the jet exit Mach number, M_j, was controlled to be equal to the design exit Mach number. The jet exit conditions are calculated from the isentropic relations and the dynamic viscosity is based on Sutherland's law,

$$\frac{\mu_j}{\mu_{ref}} = \left(\frac{T_j}{T_{ref}} \right)^{3/2} \frac{T_{ref} + s}{T_j + s}, \tag{4}$$

where $\mu_{ref} = 1.716 \cdot 10^{-5} \mathrm{Ns/m}^2$, $T_{ref} = 273\mathrm{K}$ and $s = 111\mathrm{K}$ for air. The experimental conditions and flow quantities at the jet exit (subscript 'j'), ambient (subscript '∞') and stagnation (subscript '0') are summarized in table 2. Additional non-dimensional variables relevant to this study are also presented.

III.   Acoustical Characteristics of the Fully Expanded Mach 3 Jet

III.A.   Statistics and Spectral Distributions

The spatial topography of the overall sound pressure level (OASPL) obtained from the planar grid measurements is presented in figure 6. Contours can also be found in the literature,[2,11] but none with a range up to $x = 145D_j$ and $r = 95D_j$. While the classical heart shape pattern and cone of silence is clearly present, it is interesting to note the straight upward ramp in OASPL centered around $\theta = 45°$ (initiating from jet exit). Tam *et al.* (1992)[12] suggests that the direction of peak sound intensity coincides with the direction of Mach cone half angle when the Mach waves become the dominant sound production mechanisms in the turbulent mixing noise. This justifies the assumption that the convective speed of the large instability waves causing Mach wave radiation is equal to $0.80U_j$ (used to compute the Mach wave radiation angle ϕ). Likewise, experimental studies by McLaughlin *et al.* (1975)[2] and Troutt and McLaughlin (1982)[9] of an excited jet show evidence of a phase velocity of the axial instability waves around $0.80U_j$ over a broad range of wave numbers. This OASPL distribution supports the notion that Mach wave radiation intensity decays rapidly across the Mach cone half angle ϕ, and, the 'edge' of Mach wave radiation at the upstream angle remains distinct with outward distance, up to (and likely beyond) the range of consideration.

Figure 7 presents the spectra along the 'artificial' arc-array and line-array. For the arc-array, the spectra are relative peaky at shallow angles ($\phi \leqslant 49.1$) and are an indication that Mach wave radiation is the prominent source. Broadband, lower amplitude, spectra are observed at sideline and upstream angles ($\phi \geqslant 57.1$) and represent the broadband nature of the fine-scale turbulence mixing noise. The trend of these far-field observations are well-known[6] and they follow the recent observations of Baars *et al.* (2011).[16]

An interesting observation that can be shown with these findings is to what effect relative humidity has on the acoustic waveform in terms of atmospheric absorption and nonlinear wave steepening. This is

Table 2. Summary of the experimental conditions during the measurements with the microphone grid-array and line-array (M_j was controlled to be the fully expanded Mach number $M_e = 3.00$).

|		grid-array (day 1)	grid-array (day 2)	line-array (day 3)
	M_j		$3.00 \pm 1\%$	
	$NPR = p_0/p_\infty$		$36.73 \pm 4.5\%$	
measured	p_∞ [kPa]	100.7	100.8	101.2
	T_0 [K]	291.2	286.2	285.1
	T_∞ [K]	293.3	287.2	287.5
	Rel. hum. [%]	75.4	63.2	48.2
calculated	T_j [K]	104.0	102.2	101.8
	a_j [m/s]	204.4	202.7	202.3
	a_∞ [m/s]	343.3	339.7	339.9
	U_j [m/s]	613.3	608.0	606.9
	$f_c = U_j/D_j$ [kHz]	24.1	23.9	23.9
	T_j/T_∞	0.35	0.36	0.35
	ρ_∞/ρ_j	0.35	0.36	0.35
	Re_j	$7.4 \cdot 10^6$	$7.6 \cdot 10^6$	$7.6 \cdot 10^6$
	$U_c = 0.80 U_j$ [m/s]	490.6	486.4	485.5
	$M_a = U_j/a_\infty$	1.79	1.79	1.79
	$M_{con} = U_c/a_\infty$	1.43	1.43	1.43
	ϕ [degr]	45.6	45.7	45.6
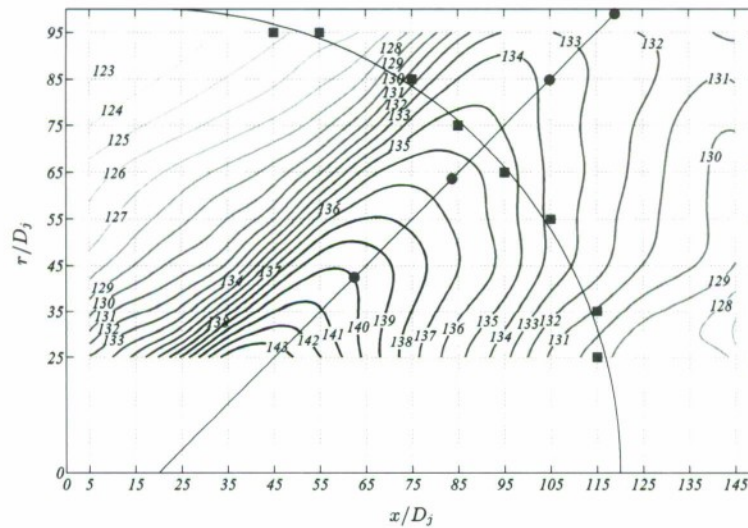
Figure 6. Contours of constant Overall Sound Pressure Level (OASPL) in dB, $p_{ref} = 20 \mu Pa$.

shown in figure 8. Each pair of spectra, grey and black, are acquired at the same x, r location but on different days under different environmental conditions (relative humidity). Higher humidity affects the spectra considerably by damping out the small scale fluctuations, all the while amplifying the contribution of the N-wave patterns to the raw pressure waveform.
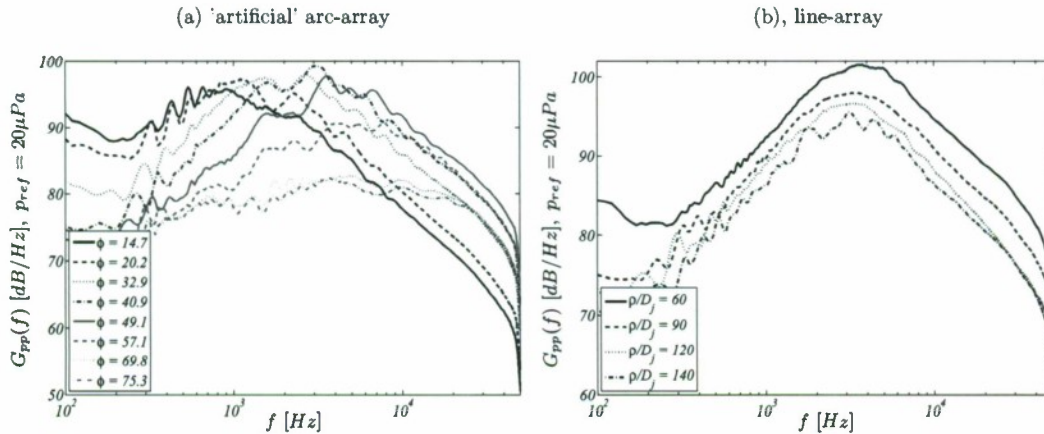
Figure 7. One-sided power spectral densities (5% bandwidth moving filter applied).
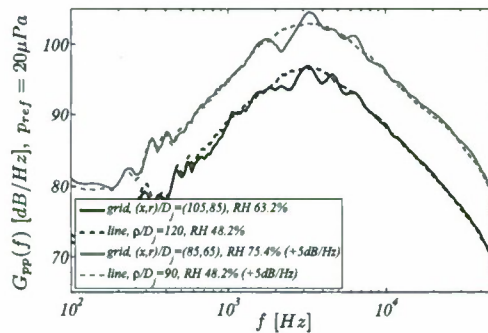

Figure 8. One-sided power spectral densities indicating the 'wiggles' in the spectra for high relative humidity conditions.

Contour plots of the sound intensity at various Strouhal numbers are presented in figure 9. Due to the atmospheric absorption effects discussed in figure 6, a 20% bandwidth average filter was applied around each center frequency. At low frequencies, figure 9a, the peak intensity direction is shallower than $\phi = 45°$ and is related to a considerable drop in the axial phase velocity of the instability waves for low frequencies ($St < 0.2$).[9] Shallow propagation of low frequency noise was also observed by Kuo *et al.* (2010).[24]

For the higher frequencies, figures 9b-f, the peak radiation angle is fairly constant at 45°. The position, however, shifts upstream for higher frequencies. In general, this finding supports the notion that high frequency noise radiates from regions close to the nozzle exit, while low frequency noise dominates locations further downstream. Kuo *et al.* (2010)[24] also observed that the angular orientation of the lobe of peak intensity remained mostly unchanged with frequency for a cold supersonic jet. Opposite to the current result, Kuo *et al.* (2010)[24] observed a broadening of the lobe at higher frequencies and concluded that this is consistent with the more omni-directional pattern of fine-scale turbulence noise. Here, a broadening is not explicitly observed. A plausible explanation for this discrepancy is the high convective Mach number in this study, since that causes the directional Mach wave radiation to saturate more of the higher frequency omni-directional sound waves. Henceforth, any acoustic field differences, from for example subsonic/transonic jets, might express themselves better due to the high convective (1.43) and acoustic (1.79) Mach number compared to most supersonic jet studies where the acoustic Mach number is around 1 and the convective Mach number is mostly subsonic. Any typical trends can then be saturated by more conventional sound
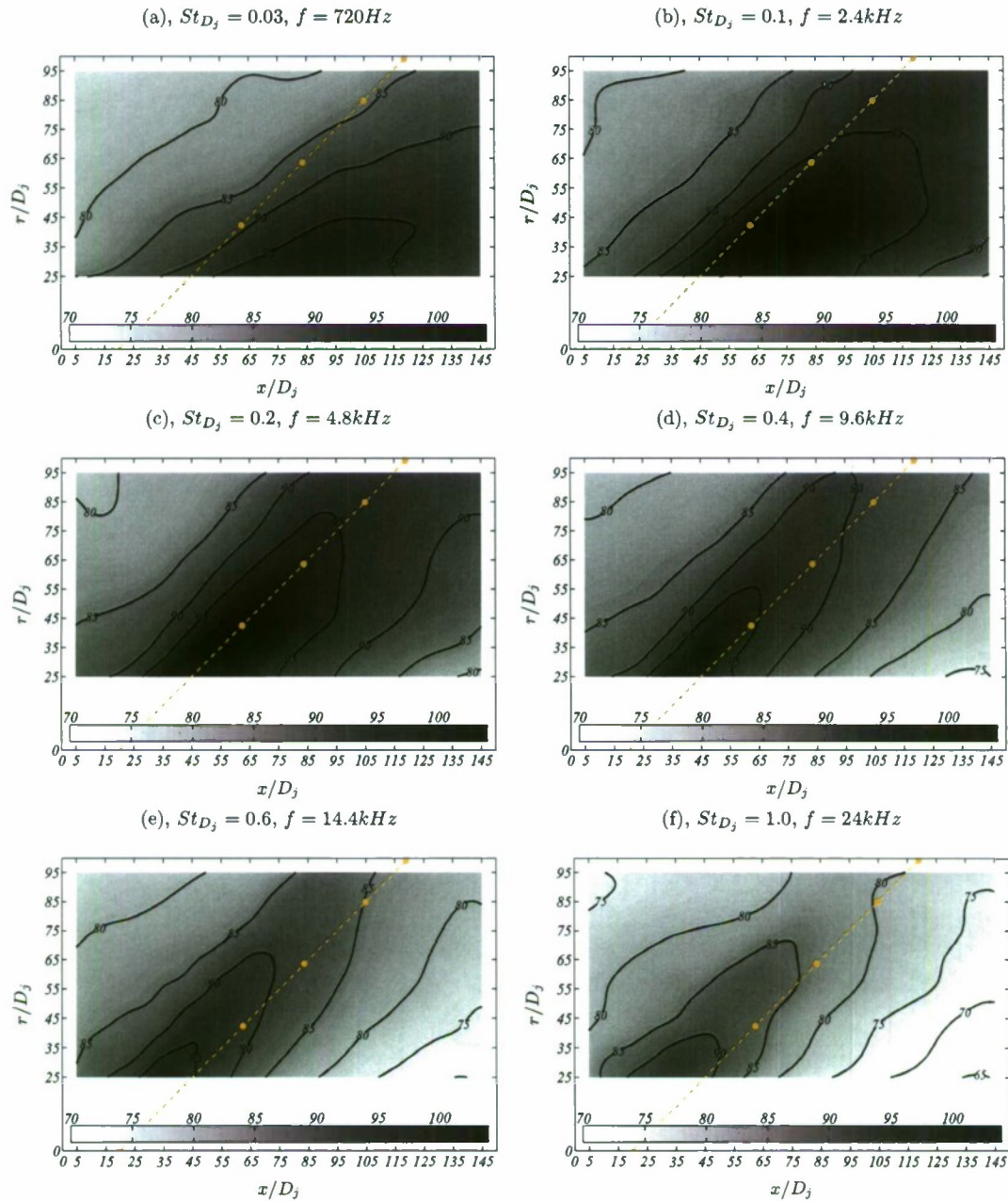
Figure 9. Contours of the SPL centered around specific Strouhal numbers (frequencies) with a bandwidth of ±20%.

producing mechanisms. And thus, while the low frequency distributions are dominated by the directional Mach wave radiation as is expected, the high frequency content (up to $St_{D_j} = 1.0$) is found to be directional

too in the case of this Mach 3 jet.

III.B. Measures of Nonlinearity for Wave Propagation to the Far-Field

Two measures of the nonlinearity in the pressure waveforms are displayed in figure 10: the Skewness of the pressure derivative and the WSF. Both are presented in a normalized form such that 10 is the peak value and a higher number represents more nonlinearity. Their spatial distributions suggest the presence of wave steepening at a preferred direction of around 45° which is closely aligned with the direction of highest sound intensity and Mach wave radiation. A steep upward ramp is observed in the field of both criteria, matching the upward ramp as was discussed for the OASPL (figure 6). Although the trends are globally equal for both criteria, the difference manifests itself when the peak location is considered. The maximum nonlinearity occurs upstream of the line-array according to the WSF criterion and downstream for the Skewness criterion. The physical relevance of the nodes are questionable given the proximity of the chamber wall and wind tunnel collector to these measurement locations. This is currently being investigated. The PDF's of the pressure derivative for 4 microphones along the line-array are presented in figure 11 for reference.
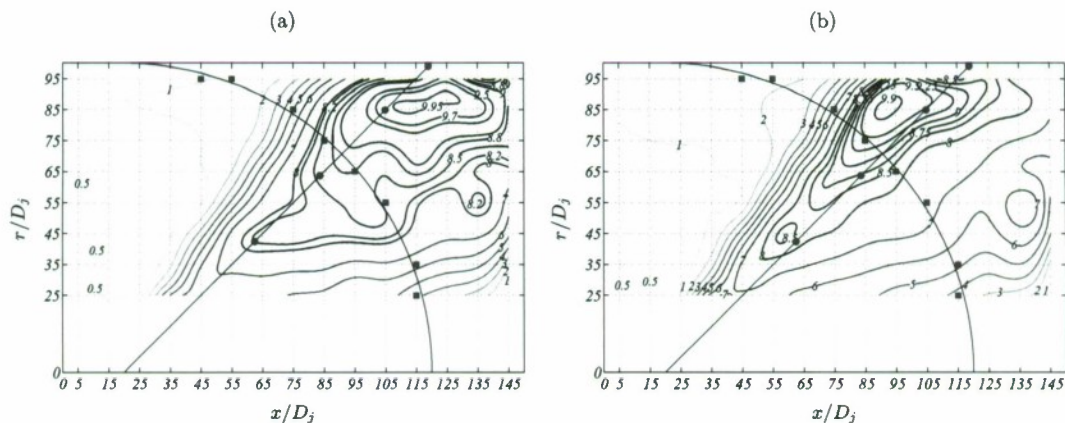
(a)   (b)

Figure 10. (a), Contour of the normalized Skewness, $S/S_{max} \times 10$, **where** $S_{max} = 1.96$ **at position** $(x, r)/D_j = (115, 85)$, **(b), Contour of the normalized Wave Steepening Factor (WSF),** $(1 - WSF)/(1 - WSF)_{max} \times 10$, **where** $(1 - WSF)_{max} = 0.36$ **at position** $(x, r)/D_j = (95, 85)$.

The last nonlinearity criterion considered, the number of zero crossings per unit time, is presented in figure 12a. It is normalized such that a higher value means fewer zero crossings. A high-pass frequency filter of $300Hz$ was applied to the data to ensure a correct computation of Z_c. The result is very similar to a contour of low frequency content. Low frequency signals simply have fewer zero crossings than signals dominated by high frequency content, and therefore, this finding is not surprising. Nonetheless, an interesting conclusion can be made. Figure 12b indicates the alignment of zero crossing contours with spherically spreading paths originating from $x = 20D_j$. This implies an absence of shock coalescence along propagation paths for the relative small range considered (in terms of typical distances over which shock coalescence occurs).

IV. Wave Propagation along the Line-Array

IV.A. Basic Acoustic Features along the Line-Array

The microphones along the line-array coinciding with the direction of highest sound and Mach wave radiation intensity were acquired synchronously for correlation and waveform analyses. The PDF's of the pressure waveform derivatives are shown in figure 13a for respectively all four microphones. Although the standard deviation of these decreases with outward distance, the skewness factor increases, and so, nonlinear effects become more pronounced along the array as was discussed in section III.B. The arrival times of the acoustic disturbances are computed from the temporal cross correlations (figure 13b) between the first ($60D_j$) and

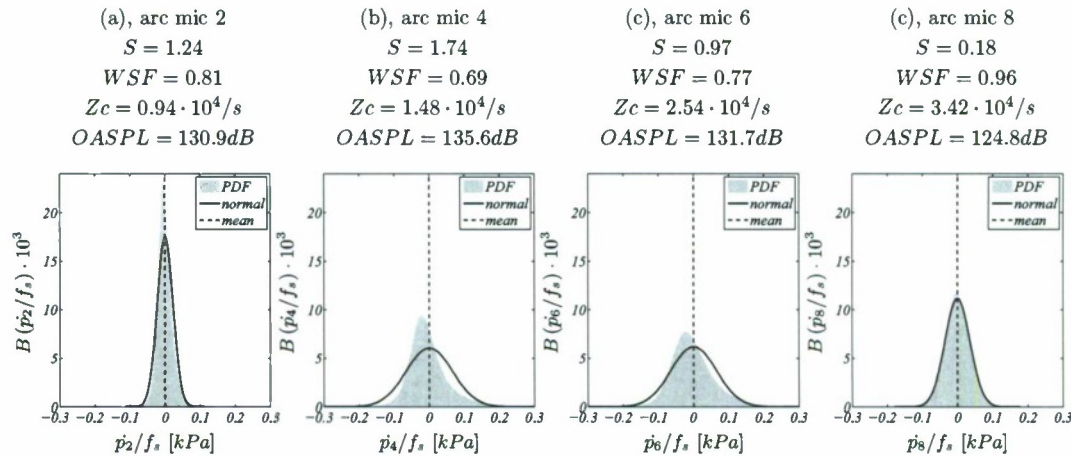| (a), arc mic 2	(b), arc mic 4	(c), arc mic 6	(c), arc mic 8
$S = 1.24$	$S = 1.74$	$S = 0.97$	$S = 0.18$
$WSF = 0.81$	$WSF = 0.69$	$WSF = 0.77$	$WSF = 0.96$
$Zc = 0.94 \cdot 10^4/s$	$Zc = 1.48 \cdot 10^4/s$	$Zc = 2.54 \cdot 10^4/s$	$Zc = 3.42 \cdot 10^4/s$
$OASPL = 130.9dB$	$OASPL = 135.6dB$	$OASPL = 131.7dB$	$OASPL = 124.8dB$

Figure 11. Probability Density Functions (PDF) of the derivative of the temporal pressure waveforms at four locations on the arc-array (a corresponding normal distribution is indicated for reference).
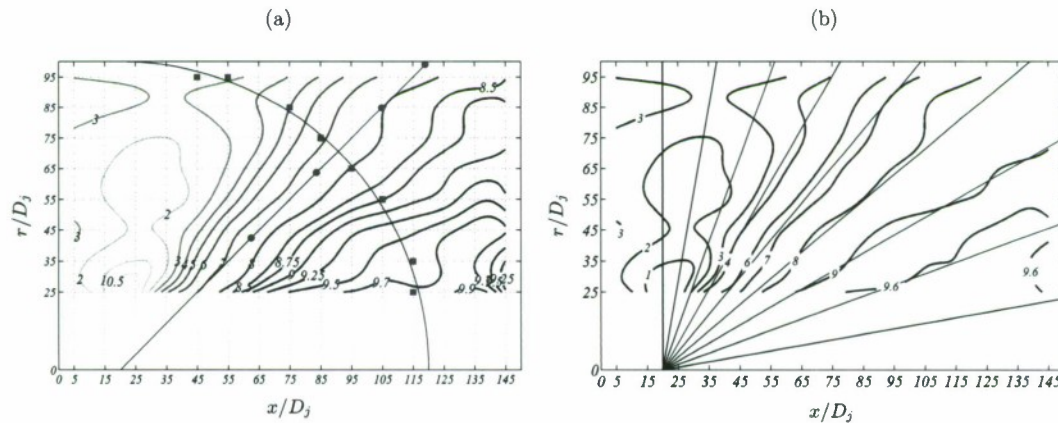
(a)   (b)

Figure 12. (a), Contour the number of zero crossings in the form $(Zc_{max} - Zc)/(Zc_{max} - Zc)_{max} \times 10$, where $Zc_{max} = 4.25 \cdot 10^4/s$ at position $(x,r)/D_j = (25,25)$ and $(Zc_{max} - Zc) = 3.44 \cdot 10^4/s$ at position $(x,r)/D_j = (135,25)$, (b), Spherical rays spreading from $(x,r)/D_j = (20,0)$ lining up with lines of constant number of zero crossings.

three remaining microphones. Dividing the distance between microphones by the associated travel time results in the ambient sound speed within 0.4%. The linear coherence spectra between line-array microphones are presented in figure 14.

IV.B. Application of the Numerical Prediction Algorithms

To determine the effect of nonlinearity in the propagation of the noise, the time waveform recorded at a distance of $60Dj$ was used as the input condition to the hybrid time-frequency Burgers solution algorithm previously described. The algorithm sequentially calculates the solution to the standard, nonlinear Burgers equation and then the linearized Burgers equation.
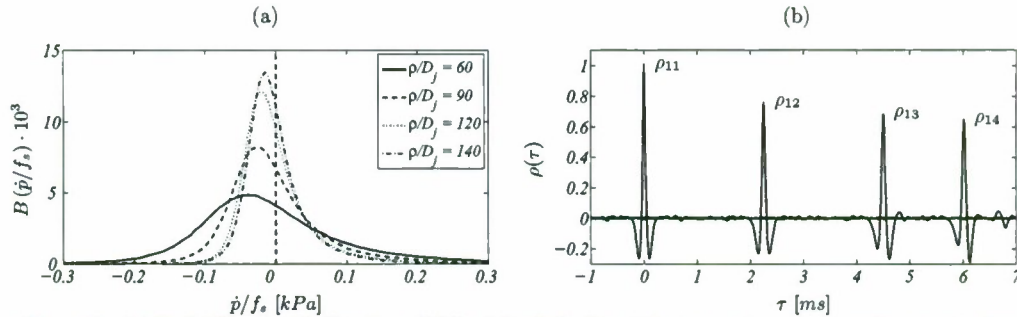
American Institute of Aeronautics and Astronautics

Figure 13. (a) Probability Density Functions (PDF) of the derivative of the temporal pressure waveforms at the four locations on the line-array, (b) The temporal cross correlation coefficient between the microphones on the line-array.
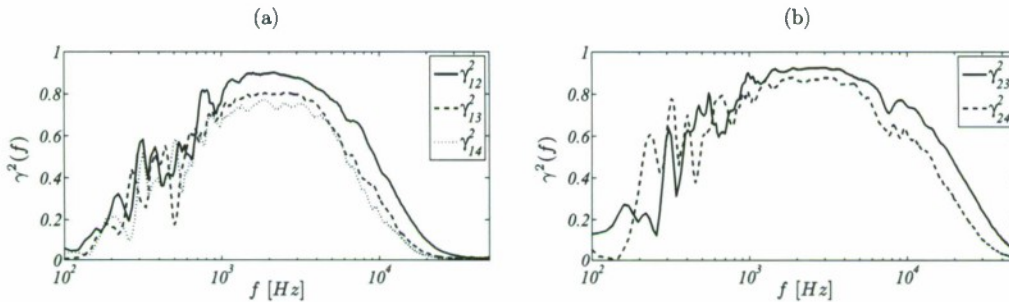

Figure 14. Linear coherence spectra between the microphones on the line-array (5% bandwidth moving filter applied).

IV.C. Spectral Comparison

Figure 15a shows a comparison between the predicted linear and nonlinear spectra at $140Dj$ compared to the input spectrum which was recorded at $60Dj$. One significant difference between the two predictions is the greater amount of power at high frequencies for the nonlinear case, which is expected since wave steepening continues along the propagation path. The increase in high frequency energy comes at the expense of a decrease in peak frequency energy. The linear prediction, meanwhile, is qualitatively very similar to the input spectrum, and this is due to the fact that the linear propagation model simply applies geometrical spreading, absorption and dispersion losses to the waveform, which in this case corresponds to essentially a decrease in energy across the frequency spectrum.

Figure 15b shows a direct comparison between the predicted and measured spectra at $140Dj$. The difference in high frequency energy between the measured signal at $140Dj$ and the nonlinear prediction still exists, which means one of two things: either wave steepening has terminated after $60Dj$ or the measurement system is not capable of measuring the frequencies that the algorithm is predicting (limitations are the $1/4in$ microphones and the sampling rate). Considering that figure 10 demonstrates that the skewness and wave steepening factor are increasing past the $60Dj$ point, it is reasonable to assume that wave steepening is still occurring and that the reason for the lack of agreement between the measured spectra and nonlinear prediction is an inability to measure such high frequencies.

IV.D. Temporal Waveform Comparison

Finally, figure 16 compares the measured time waveforms at $60Dj$ and $140Dj$ to the linear and nonlinear time waveform predictions. Figure 16a shows the linear prediction and the effect of the simple frequency domain filter that is applied to the waveform, which accounts for geometrical spreading and atmospheric absorption
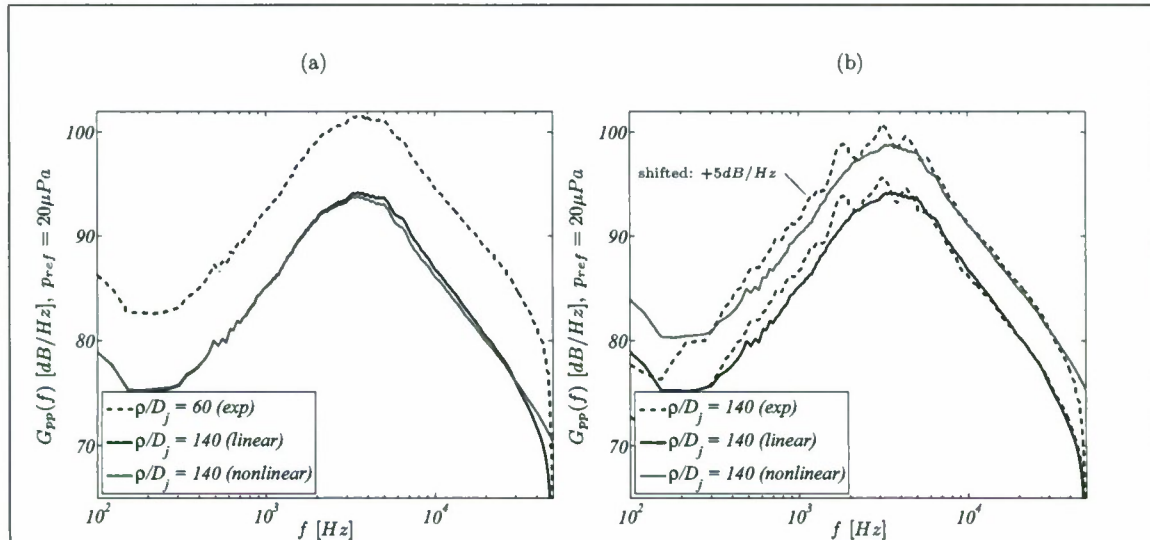
Figure 15. (a) Predictions of the one-sided power spectral densities at $\rho/D_j = 140$ as well as the power spectral density of the input waveform at location $\rho/D_j = 60$, (b) Comparison of the predicted and measured spectra at location $\rho/D_j = 140$ (5% bandwidth moving filter applied).

losses, including the effects of molecular relaxation. Over the short propagation distance considered here, the fact that the atmospheric absorption and dispersion is frequency-dependent does not make itself apparent, and generally the effect is a simple decrease in pressure amplitude. Figure 16b shows how the nonlinear algorithm predicts continued wave steepening in the face of losses due to spreading and absorption, and this was increase in high-frequency energy was also visible in the spectra shown in figure 15. Figure 16c shows a direct comparison between the two predictions and the actual time waveform recorded at $140Dj$. Focusing on the peak residing at approximately 0.7ms, it is apparent that the linear prediction is a closer match than the nonlinear prediction, but again this may be due to an inability to measure such high-frequency shocks. Also of note is the peak at approximately 0.9ms, which was likely due to energy propagating from a different source location than the $60Dj$ position. The algorithm used assumes that all energy is propagating spherically outward from the input time waveform position, and in this case, it is evident that not all energy does.

Acknowledgements

References

[1] Tam, C. K. W., Pastouchenko, N. N., and Viswanathan, K., "Fine-Scale Turbulence Noise from Hot Jets," *AIAA Journal*, Vol. 43, No. 8, Aug. 2005, pp. 1675–1683.

[2] McLaughlin, D. K., Morrison, G. L., and Troutt, T. R., "Experiments on the instability waves in a supersonic jet and their acoustic radiation," *Journal of Fluid Mechanics*, Vol. 69, 1975, pp. 73–95.

[3] Seiner, J. M., Bhat, T. R. S., and Ponton, M. K., "Mach Wave Emission from a High-Temperature Supersonic Jet," *AIAA Journal*, Vol. 32, No. 12, 1994, pp. 2345–2350.

[4] Tam, C. K. W. and Chen, P., "Turbulent Mixing Noise from Supersonic Jets," *AIAA Journal*, Vol. 32, No. 9, Sept. 1994, pp. 1774–1780.
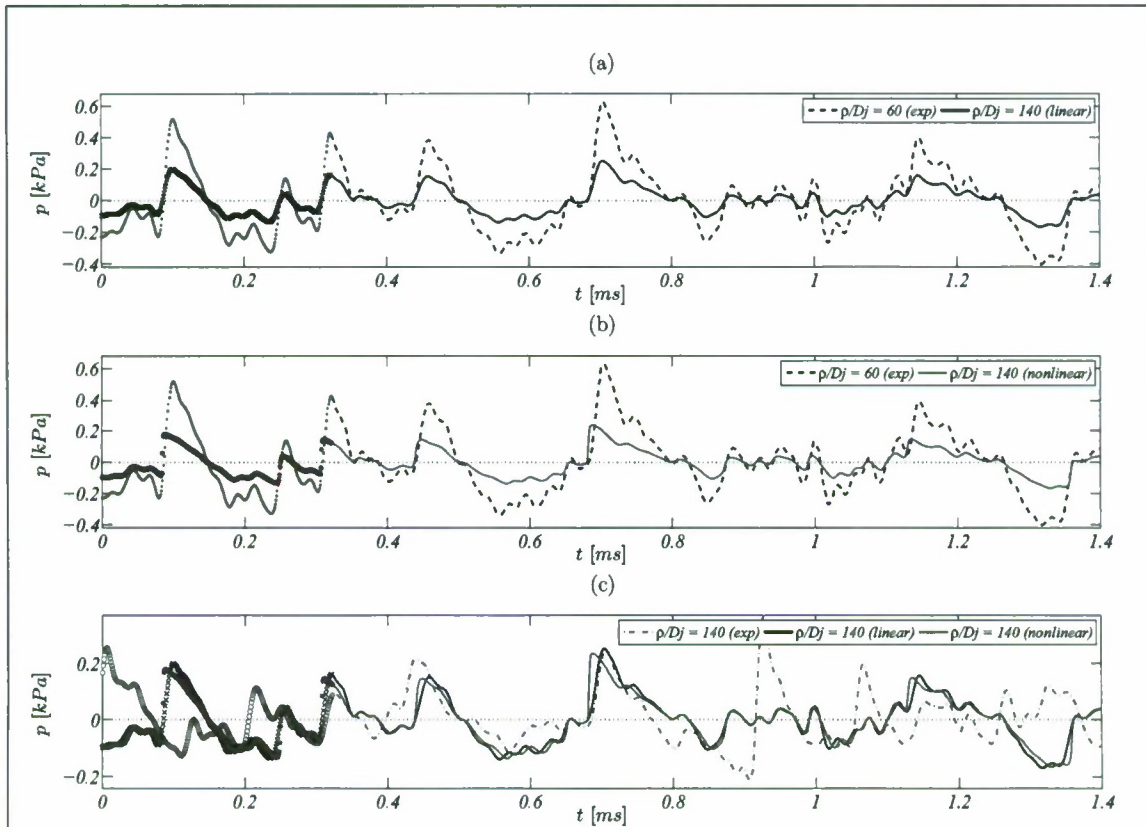
Figure 16. Temporal pressure waveforms of the experiment and the linear and nonlinear numerical predictions.

[5]Tam, C. K. W., Viswanathan, K., Ahuja, K. K., and Panda, J., "The sources of jet noise: experimental evidence," *Journal of Fluid Mechanics*, Vol. 615, 2008, pp. 253–292.

[6]Tam, C. K. W., "Mach Wave Radiation from High-Speed Jets," *AIAA Journal*, Vol. 47, No. 10, Oct. 2009, pp. 2440–2448.

[7]Tanna, H. K. and Dean, P. D., "The Influence of Temperature on Shock-Free Supersonic Jet Noise," *Journal of Sound and Vibration*, Vol. 39, No. 4, 1975, pp. 429–460.

[8]Morris, P. J., "Flow Characteristics of the Large Scale Wave-Like Structure of a Supersonic Round Jet," *Journal of Sound and Vibration*, Vol. 53, No. 2, 1977, pp. 223–244.

[9]Troutt, T. R. and McLaughlin, D. K., "Experiments on the flow and acoustic properties of a moderate-Reynolds-number supersonic jet," *Journal of Fluid Mechanics*, Vol. 116, 1982, pp. 123–156.

[10]Crighton, D. G. and Bashforth, S., "Nonlinear Propagation of Broadband Jet Noise," *6th AIAA Aeroacoustics Conference*, AIAA, Hartford, CT, June 1980.

[11]Gallagher, J., "The Effect of Non-Linear Propagation in Jet Noise," *20th Aerospace Sciences Meeting and Exhibit*, AIAA, Orlando, Florida, Jan. 1982.

[12]Tam, C. K. W., Chen, P., and Seiner, J. M., "Relationship Between Instability Waves and Noise of High-Speed Jets," *AIAA Journal*, Vol. 30, No. 7, jul 1992, pp. 1747–1752.

[13]Bridges, J., "Effect of Heat on Space-Time Correlations in Jets," *12th AIAA/CEAS Aeroacoustics Conference*, AIAA, Cambridge, Massachusetts, May 2006.

[14]Bridges, J. and Wernet, M. P., "Effect of Temperature on Jet Velocity Spectra," *13th AIAA/CEAS Aeroacoustics Conference*, AIAA, Rome, Italy, May 2007.

[15]McLaughlin, D. K., Bridges, J. E., and Kuo, C.-W., "On the scaling of small, heat simulated jet noise measurements to moderate size exhaust jets," *16th AIAA/CEAS Aeroacoustics Conference*, AIAA, Stockholm, Sweden, June 2010.

[16]Baars, W. J., Tinney, C. E., Murray, N. E., Jansen, B. J., and Panickar, P., "The Effect of Heat on Turbulent Mixing Noise in Supersonic Jets," *49th Aerospace Sciences Meeting and Exhibit*, AIAA, Orlando, Florida, Jan. 2011, AIAA Paper 2011-1029.

[17] Morris, P. J., "A note on noise generation by large scale turbulent structures in subsonic and supersonic jets," *International Journal of Aeroacoustics*, Vol. 8, No. 4, 2009, pp. 301–316.

[18] Petitjean, B. P., Viswanathan, K., and McLaughlin, D. K., "Acoustic pressure waveforms measured in high speed jet noise experiencing nonlinear propagation," *International Journal of Aeroacoustics*, Vol. 5, No. 2, 2006, pp. 193–215.

[19] Gee, K. L., Sparrow, V. W., James, M. M., Downing, J. M., Hobbs, C. M., Gabrielson, T. B., and Atchley, A. A., "The role of nonlinear effects in the propagation of noise from high-power jet aircraft," *Journal of Acoustical Society of America*, Vol. 123, No. 6, 2008, pp. 4082–4092.

[20] Pestorius, F. M. and Blackstock, D. T., "Propagation of finite-amplitude noise," *Finite-amplitude wave effects in fluids, Proceedings of the 1973 Symposium*, 1973.

[21] Hamilton, M. F. and Blackstock, D. T., *Nonlinear Acoustics*, Acoustical Society of America, Melville, NY, 2008.

[22] Howell, G. P. and Morfey, C. L., "Non-Linear Propagation of Broadband Noise Signals," *Journal of Sound and Vibration*, Vol. 114, No. 2, 1987, pp. 189–201.

[23] Gee, K. L., Shepherd, M. R., Falco, L. E., Atchley, A. A., Ukeiley, L. S., Jansen, B. J., and Seiner, J. M., "Identification of Nonlinear and Near-field Effects in Jet Noise Using Nonlinearity Indicators," *13th AIAA/CEAS Aeroacoustics Conference*, AIAA, Rome, Italy, May 2007, AIAA Paper 2007-3653.

[24] Kuo, C.-W., Veltin, J., and McLaughlin, D. K., "Effects of Jet Noise Source Distribution on Acoustic Far-Field Measurements," *48th Aerospace Sciences Meeting and Exhibit*, AIAA, Orlando, Florida, Jan. 2010, AIAA Paper 2010-474.

[25] Gee, K. L., Atchley, A. A., Falco, L. E., Gabrielson, T. B., and Sparrow, V. W., "Bispectral Analysis of High-Amplitude Jet Noise," *11th AIAA/CEAS Aeroacoustics Conference*, AIAA, Monterey, California, May 2005.

[26] Tick, L. J., "The Estimation of "Transfer Functions" of Quadratic Systems," *Technometrics, IEEE*, Vol. 3, No. 4, Nov. 1961, pp. 563–567.

[27] Baars, W. J., Tinney, C. E., and Powers, E. J., "POD based spectral Higher-Order Stochastic Estimation," *48th Aerospace Sciences Meeting and Exhibit*, AIAA, Orlando, Florida, Jan. 2010, AIAA Paper 2010-1292.

[28] Tennekes, H. and Lumley, J. L., *A First Course in Turbulence*, The MIT Press, Cambridge, Massachusetts, 1972.